Contract No:

This document was prepared in conjunction with work accomplished under Contract No. DE-AC09-08SR22470 with the U.S. Department of Energy (DOE) Office of Environmental Management (EM).

Disclaimer:

This work was prepared under an agreement with and funded by the U.S. Government. Neither the U. S. Government or its employees, nor any of its contractors, subcontractors or their employees, makes any express or implied:

1) warranty or assumes any legal liability for the accuracy, completeness, or for the use or results of such use of any information, product, or process disclosed; or
2) representation that such use or results of such use would not infringe privately owned rights; or
3) endorsement or recommendation of any specifically identified commercial product, process, or service.

Any views and opinions of authors expressed in this work do not necessarily state or reflect those of the United States Government, or its contractors, or subcontractors.

Characterization of Unsaturated Hydraulic Conductivity in Fractured Media Using the Multistep Outflow Method

G. P. Flach

K. L. Dixon

F. G. Smith III

R. L. Nichols

SRNL.DOE.GOV

DISCLAIMER

Characterization of Unsaturated Hydraulic Conductivity in Fractured Media Using the Multistep Outflow Method

G. P. Flach
K. L. Dixon
F. G. Smith III
R. L. Nichols

April 2015

Savannah River National Laboratory™

OPERATED BY SAVANNAH RIVER NUCLEAR SOLUTIONS

iii

REVIEWS AND APPROVALS

AUTHORS:

_____
G. P. Flach, Radiological Performance Assessment   Date

_____
K. L. Dixon, Geosciences   Date

_____
F. G. Smith III, Radiological Performance Assessment   Date

_____
R. L. Nichols, Geosciences   Date

TECHNICAL REVIEW:

_____
L. L. Hamm, National Security Studies   Date

APPROVAL:

_____
D. A. Crowley, Manager   Date
Radiological Performance Assessment

_____
T. O. Oliver, Manager   Date
Geosciences

_____
H. H. Burns, Project Manager   Date

_____
E. N. Hoffman, Manager   Date
Engineering Process Development

_____
S. L. Marra, Manager   Date
Environmental Stewardship

ACKNOWLEDGEMENTS

EXECUTIVE SUMMARY

DOE Performance Assessments often involve analysis of cementitious waste forms and barriers that are known or postulated to physically degrade over time. Physical damage resulting from local-scale degradation mechanisms is commonly assumed to take the form of small-scale cracking. Unsaturated hydraulic properties must be defined for such fractured cementitious materials, in order to simulate moisture movement and contaminant transport within and around the closure or disposal facility. Recognizing the need for an experimental technique to measure the unsaturated hydraulic properties of unsaturated fractured media, Dixon and Nichols (2013) recently applied the *multistep outflow method* to fractured cementitious materials. The multistep outflow method involves monitoring the transient flow of water extracted from a sample through a high air-entry pressure porous plate in response to step increases in gas pressure. Water retention and relative permeability curves are determined through inverse fitting of a flow simulation model to the transient outflow data. Initial testing by Dixon and Nichols (2013) with grout samples suggested that the modified apparatus/method can provide a viable means to measure the unsaturated hydraulic properties of micro-fractured cementitious materials. However, the test method had not been rigorously validated against a known standard.

In this study, the multistep outflow method of Dixon and Nichols (2013) is applied to a synthetic fracture network as an experimental method validation exercise. The synthetic fractured medium is composed of a series of glass plates shimmed at one end to produce wedge-shaped apertures. Analytic solutions for saturation and relative permeability are derived for the wedge geometry. van Genuchten / Mualem parameters defining water retention and relative permeability curves are estimated from three outflow extraction experiments. The fitted parameters from the three tests are consistent, but do not produce characteristic curves in agreement with the analytic solution. The reason for the discrepancy is unknown. A potential explanation is uncertainty in the wetting angle assumed for water on glass, due to the presence of hydrophobic tape shims, dissolved adhesive, a coating or contamination on the microscope slides used as glass plates, and/or other factor. Because of the observed discrepancies between the expected and observed behavior of the reference specimen, the technique of Dixon and Nichols (2013) could not be validated. However, neither was the method invalidated considering considerable uncertainty in the appropriate wetting angle to use in the analytic solution. Recommendations for addressing uncertainty in wetting angle are provided herein.

Notwithstanding difficulties with validating the test method, an additional fractured grout sample TR430 was tested three times with the method of Dixon and Nichols (2013). Characteristic curve parameters are estimated through inverse modeling using HYDRUS-1D. Data from the three TR430 tests are similar indicating some level of reproducibility in estimated parameters, despite variable pressure steps and durations. Existing data from samples TR436 and TR437 collected previously by Dixon and Nichols (2013) are further analyzed. Compared to soils, hydraulic conductivity as a function of suction/tension head for the fractured cementitious materials is observed to have a steeper negative slope. Assuming that lower hydraulic conductivity is conservative with respect to facility performance, these comparisons suggest that soils may serve as reasonable surrogates for damaged cementitious materials, provided their saturated conductivities are sufficiently large.

Dixon, K. L. and R. L. Nichols. *Method Development for Determining the Hydraulic Conductivity of Fractured Porous Media*. SRNL-STI-2013-00522, Rev. 0. September 2013.

TABLE OF CONTENTS

LIST OF TABLES

LIST OF FIGURES

LIST OF ABBREVIATIONS

CBP	Cementitious Barriers Partnership
DOE	Department of Energy
EM	Environmental Management
LLC	Limited Liability Company
PA	Performance Assessment
SA	Special Analysis
SRNL	Savannah River National Laboratory
SRS	Savannah River Site
vGM	van Genuchten (1980) / Mualem (1976)

1.0 Introduction

DOE Performance Assessments (PAs) and augmenting Special Analyses (SAs) often involve analysis of cementitious waste forms and barriers that are known or postulated to physically degrade over long time periods, typically extending thousands to tens of thousands of years into the future (e.g. SRR Closure & Waste Disposal Authority 2009; Savannah River Remediation LLC 2012, 2013, 2014). Degradation mechanisms may include differential settlement, seismic events, freeze-thaw cycling, steel corrosion influenced by carbonation and/or chloride ingress, alkali-silica reaction (ASR), and sulfate attack (e.g. Cementitious Barriers Partnership 2009; Langton 2010; Flach and Smith 2014). The physical damage resulting from local-scale degradation mechanisms is commonly assumed to take the form of small-scale cracking. Because physical damage is associated with an unrealized future condition, fracture attributes such as aperture, spacing, and connectivity typically take on assumed or hypothetical values to facilitate PA modeling predictions of facility performance. Unsaturated hydraulic properties must be defined for fractured cementitious materials in order to simulate moisture movement and contaminant transport within and around the facility.

Fractured media flow can be represented by a number of modeling concepts, as depicted in Figure 1-1 reproduced from Altman et al. (1996). Recent Savannah River Site (SRS) PAs and SAs conceptualize fractured cementitious materials as homogeneous continua composed of blended (or superimposed) fractions of intact matrix and fractures (Jordan et al. 2012; Jordan and Flach 2013; Flach and Taylor 2014a, b). Local hydrologic equilibrium is assumed between matrix and fractures, such that a single pair of water retention and relative permeability curves describes the behavior of the composite material. Altman et al. (1996) identify this construct as the *Composite Porosity (Equivalent Continuum)* or *Equivalent Matrix and Fracture Continuum* modeling approach (Figure 1-1). The concept is most appropriate for smaller scale fractures and steady-state flow conditions, such that local equilibrium occurs between fractures and matrix.

The composite porosity concept leads to a two-tier or double-hump relative permeability (and hydraulic conductivity) curve as a function of capillary pressure/head, as shown schematically in Figure 1-1. The shape of the composite curve is a natural result of blending individual characteristic curves, describing matrix and fracture regions that have distinctly different saturated conductivities and air-entry pressures. For further information and blending equations see Jordan and Flach (2013, Section 2.1) for example. The characteristic curves for the fracture region may be estimated from a mechanistic model of capillary water retention and film flow for an idealized fracture geometry (e.g. Or and Tuller 2000, Tuller and Or 2002). Alternatively, Pruess (1998) states that "theoretical and experimental work suggests that relative permeability and capillary pressure behavior of fractures is similar to that of highly permeable media with intergranular porosity (Pruess and Tsang, 1990; Firoozabadi and Hauge, 1990; Persoff and Pruess, 1995). Accordingly, we used the customary van Genuchten correlations, with parameters chosen as for coarse sands." Thus high-permeability granular materials are reasonable surrogates for natural fractures with rough surfaces and/or infilled with granular material. The van Genuchten (1980) / Mualem (1976) functional forms are commonly adopted to define the individual characteristic curves, but that is not required. Figure 1-2 illustrates the two-tier or double-hump nature of composite porosity hydraulic curves using two material sets and multiple blending fractions (labeled "Degradation fraction") as specific examples taken from a recent SRS Saltstone Special Analysis (Jordan and Flach 2013; Savannah River Remediation LLC 2013). Increasing levels of damage are represented by an increasing blending fraction.

While theoretical functions based on idealized configurations or high-permeability surrogate materials produce the desired qualitative behavior of fractures, experimental datasets that might be used to quantitatively validate these or develop new functions are difficult to obtain (Liu and Bodvarsson 2001) and "virtually nonexistent" (Tuller and Or 2002; Monachesi and Guarracino 2011). In a recent journal

article, Li et al. (2014) identified only Pruess and Tsang (1990), Chen (2005) and Chen and Horne (2006) as experimental data reported in the literature. Pruess and Tsang (1990) constitutes a numerical experiment and the latter studies involve two-phase air-water flow between nominally flat plates.

Recognizing the need for an experimental technique to measure the unsaturated hydraulic properties of unsaturated fractured media, Dixon and Nichols (2013) recently applied the *multistep outflow method* concept (Kool and Parker 1988; Eching and Hopmans 1993; Hopmans et al. 2002) to fractured cementitious materials. The multistep outflow method involves monitoring the transient flow of water extracted through a high air-entry pressure porous plate in response to step increases in gas pressure. Water retention and relative permeability curve (e.g. van Genuchten) parameters are determined through inverse fitting of a Richards equation flow simulation model to the transient outflow data. HYDRUS-1D (Šimůnek et al. 2008) is commonly chosen as the inverse modeling software. The technique has become well established for characterizing soils, although parameter uniqueness and uncertainty are issues inherent with inverse modeling and obtaining accurate measurements is a persistent challenge.

Compared to typical soils, fractured media exhibit higher saturated conductivity and lower air-entry pressure, and the volume of fluid extractable from fractures is much lower than pore volumes. To accommodate these material differences, Dixon and Nichols (2013) modified a multistep outflow method apparatus suitable for soils testing by incorporating a higher conductivity ceramic pressure plate, a high-precision digital balance for logging outflow mass, a low volume (diameter) effluent line, multiple inline high-precision gas regulators, and a high-precision low range pressure gauge. Testing by Dixon and Nichols (2013) with SRS Saltstone grout samples suggests that the modified apparatus/method can provide a viable means to measure the unsaturated hydraulic properties of micro-fractured cementitious materials. However the accuracy and uniqueness of inverse modeling results are limited by inherent characteristics of fractured media: high saturated conductivity, low air-entry pressure, and strong non-linearities. Furthermore, the test method has not been rigorously validated against a known standard.

In this study, the multistep outflow method of Dixon and Nichols (2013) is applied to a synthetic fracture network with known water saturation and unsaturated hydraulic conductivity curves as a method validation exercise. Additional testing on micro-cracked saltstone samples is reported. Finally, the previous and present experimental data are further analyzed using multiple inverse model fitting approaches.
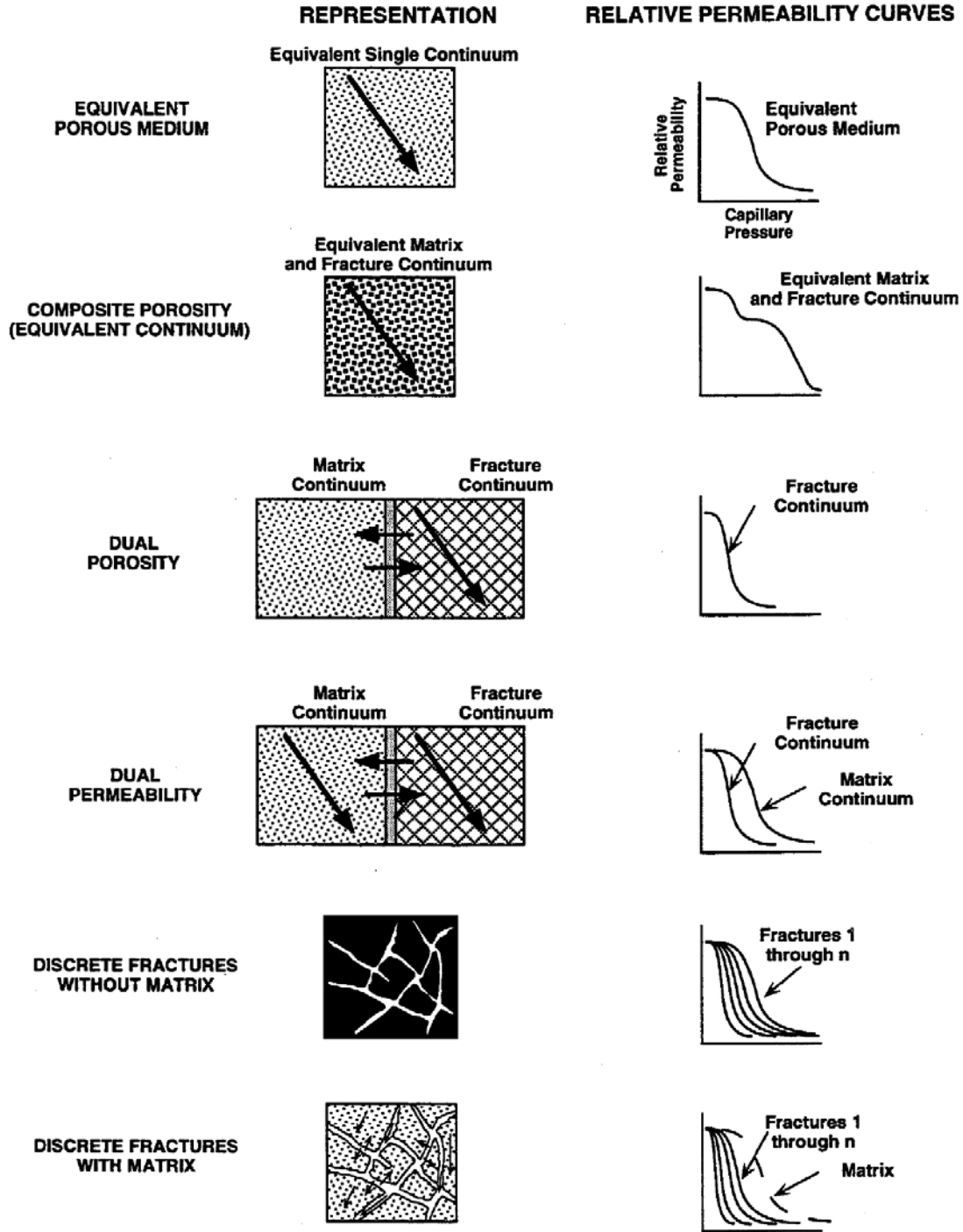
Figure 1-1. Alternative representations of a fractured medium; reproduced from Altman et al. (1996, Figure 2-2).
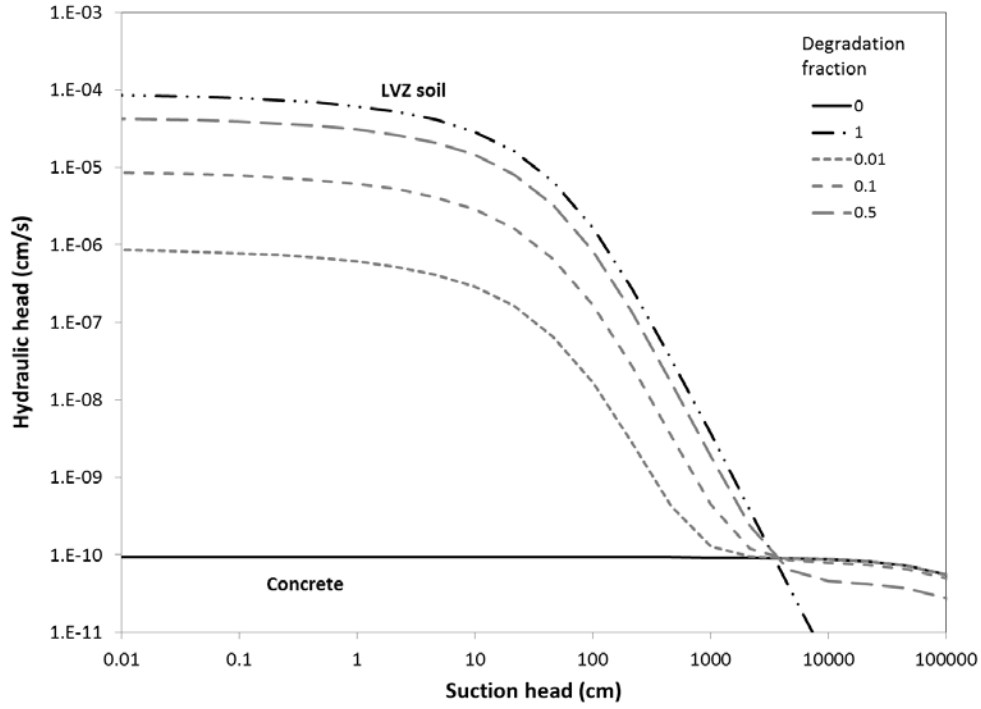
(a)
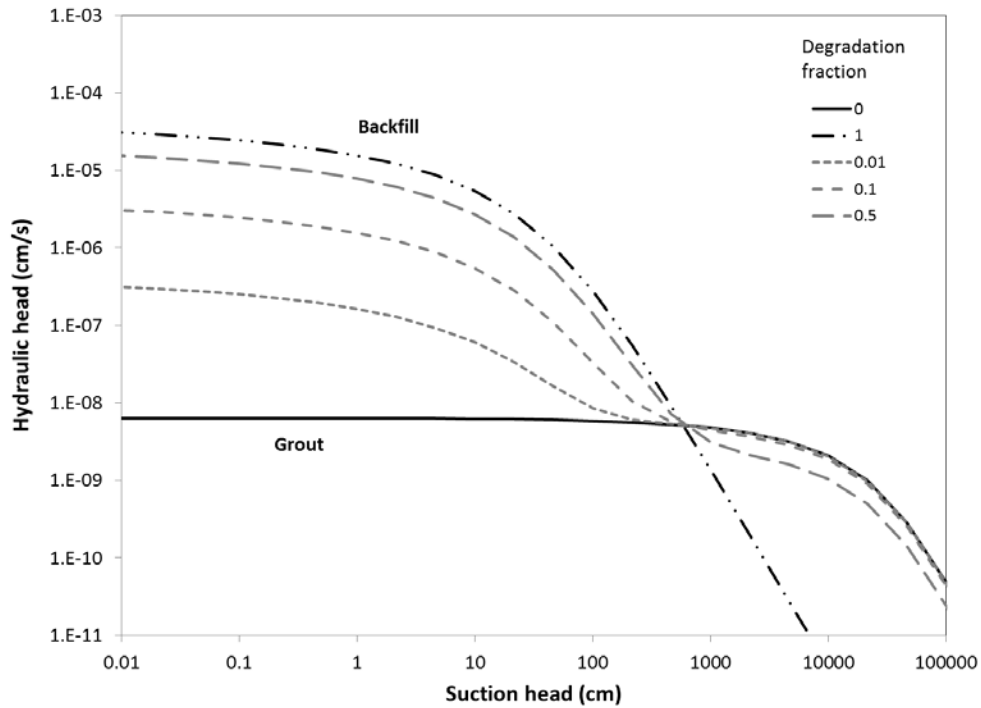
(b)

Figure 1-2. Example transitions of intact cementitious materials from intact to fully-degraded conditions represented by soils: (a) SDU 2 concrete and LVZ soil, and (b) grout and backfill soil; reproduced from Jordan and Flach (2013).

2.0 Synthetic Fractured Medium

Capillary tension in a fracture varies with geometry, particularly aperture, among other factors. For example, the capillary rise h [m] or tension between parallel plates with aperture b [m] is

$$h = \frac{2\sigma cos(\varphi)}{\rho g b} \qquad (1)$$

where σ = surface tension [N/m], φ = contact or wetting angle [rad], ρ = density [kg/m^3] and g = gravitational acceleration [m/s^2] (e.g. Wang and Narasimhan 1985). The surface tension of water is 0.07275 N/m at 20°C (Vargaftik et al. 1983). A typical wetting angle for water on glass is 25 degrees (e.g. Sumner et al. 2004, Table 2; Prakash, S. and J. Yeom 2014, Figure 3.5) but may range from 14 to 51 degrees according to Li (2008. p.70).

A natural, rough-walled, fracture network would exhibit a range of aperture sizes. A synthetic fractured medium, acting as a similar surrogate medium for test method validation, could be constructed as a collection of parallel plates with varying gaps. However, the distribution of aperture sizes would be discrete and a large number of apertures might be required to adequately emulate the behavior of a natural fracture system. A more continuous distribution can be readily constructed from apertures in the form of the wedge geometry shown in Figure 2-1. The geometry can be practically constructed using glass plates, such as microscope slides, that are in contact at one end and shimmed at the other. Furthermore, the geometry is amenable to analytic solutions.
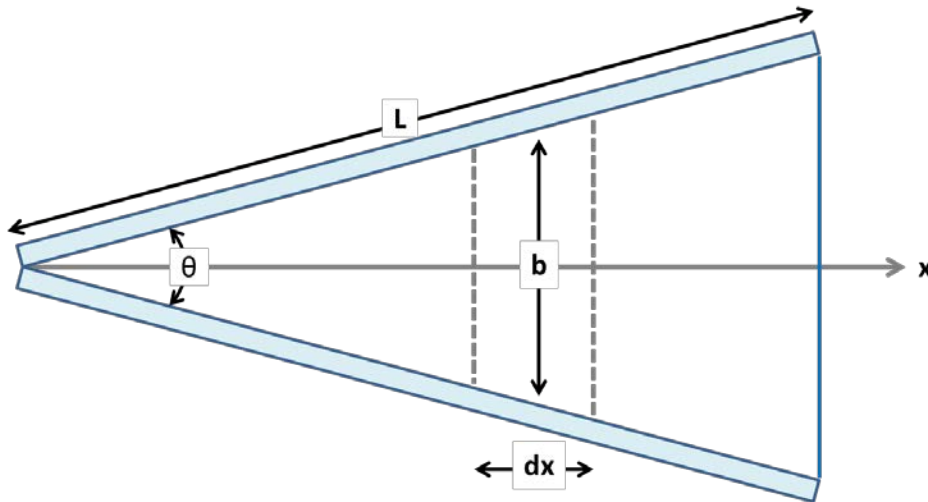
Figure 2-1. Wedge-shaped gap between two planes at an angle.

Capillary rise in a wedge forms a hyperbola (Taylor 1712; Hauksbee 1712) following Equation (1), where b now varies with the distance x from the closed end of the wedge. For planar sides of length L [m] that are separated by angle θ, the fracture length is

$$x_L = Lcos(\theta/2) \qquad (2)$$

The aperture varies with position as

$$b(x) = 2tan(\theta/2) \cdot x \qquad (3)$$

At equilibrium the capillary rise above a pool of water at zero gage pressure, or equivalently the liquid tension head ψ [m], is

$$h = \frac{2\sigma cos(\varphi)}{\rho g b(x)} = \psi \qquad (4)$$

This relationship is schematically depicted in Figure 2-2. Also shown are boxes representing plates of finite length L and height H [m] forming a physical wedge (for example a glass microscope slide). A plate in contact with a pool of water at zero gage pressure corresponds to the bottom of a box aligned with the base of the h (or ψ) axis in Figure 2-2. If the bottom of a wedge gap is in contact with liquid under tension head ψ_0 [m], then the capillary rise will be reduced by the amount. This boundary condition is depicted in Figure 2-2 by the three boxes draw at varying heights above the zero pressure baseline. Letting $z = 0$ correspond to the base of a plate, the capillary rise z_c relative to the plate bottom is

$$z_c = h - \psi_0 \qquad (5)$$
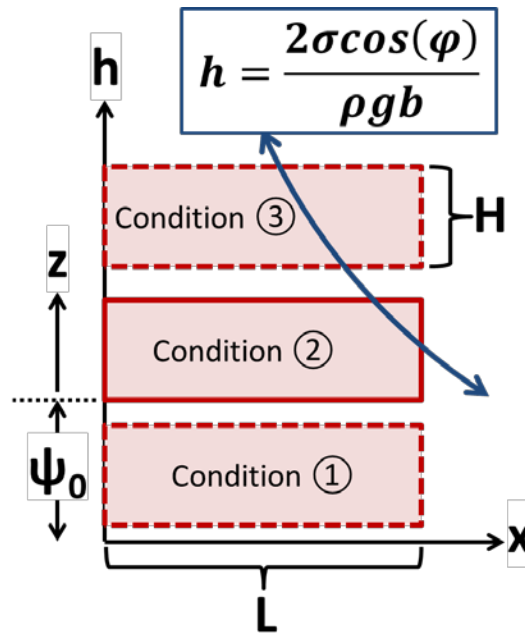
Figure 2-2. Capillary rise in a wedge-shaped fracture.

Combining Equations (3) through (5) yields the following relationship between capillary rise and position for a specified suction head at the base of the wedge

$$z_c = \frac{\sigma cos(\varphi)}{\rho g tan(\theta/2)x} - \psi_0 \equiv \frac{B}{x} - \psi_0 \qquad (6)$$

The parameter B [m^2] defined as

$$B = \frac{\sigma cos(\varphi)}{\rho g tan(\theta/2)} \tag{7}$$

is a constant for given plate material, fluid and wedge angle. The parameter z_c can also be identified as the *critical height* above which the gap is no longer liquid filled. Similarly, the *critical position* x_c [m] beyond which the gap is no longer liquid filled at a given elevation z is

$$x_c = \frac{B}{\psi_0 + z} \tag{8}$$

Liquid may occupy a finite wedge gap in the three distinct configurations shown in Figure 2-2. Configuration ① is a completely liquid filled gap and occurs when tension head at the base satisfies

$$\textit{Configuration ①:} \qquad\qquad \psi_0 < \frac{B}{x_L} - H \tag{9}$$

Configuration ② is defined by the gap being saturated at the base and unsaturated at the top. This configuration occurs when

$$\textit{Configuration ②:} \qquad\qquad \frac{B}{x_L} - H < \psi_0 < \frac{B}{x_L} \tag{10}$$

Configuration ③ corresponds to the liquid line crossing both the upper and lower boundaries of the finite wedge gap, which occurs when

$$\textit{Configuration ③:} \qquad\qquad \psi_0 > \frac{B}{x_L} \tag{11}$$

The transition between Configuration ① and Configuration ② is the transition from saturated to unsaturated conditions. Thus the air-entry pressure head for the wedge gap is defined by

$$\textit{Air-entry pressure:} \qquad\qquad \psi_{air-entry} = \frac{B}{x_L} - H \tag{12}$$

based on Equations (9) and (10). The volume of the finite wedge-shaped gap is derived through direct integration using Equation (3) as

$$V = \int_0^H \int_0^{x_L} b(x) dx\, dz = tan(\theta/2) x_L^2 H \tag{13}$$

For Configuration ① the liquid filled volume V^w is obviously

$$V^w = V = tan(\theta/2) x_L^2 H \tag{14}$$

and thus

$$S \equiv V^w/V = 1 \tag{15}$$

as expected. The saturation state of the other two configurations can be derived through straightforward, although somewhat tedious, integration.

Depending of the order of spatial integration for V_w, the horizontal and vertical areas occupied by water can be computed first for convenience. The horizontal water area

$$A_h^w = \int_0^{min(x_c,x_L)} b(x)dx \tag{16}$$

Direct integration using Equation (3) yields

$$A_h^w(z) = tan(\theta/2)min(x_c^2, x_L^2) = tan(\theta/2)min\left[\left(\frac{B}{\psi_0 + z}\right)^2, x_L^2\right] \tag{17}$$

Equation (17) is valid for all three configurations shown in Figure 2-2. The vertical water area is

$$A_v^w = \int_0^{min[max(0,z_c),H]} b(x)dz \tag{18}$$

Direct integration using Equation (3) yields

$$\begin{aligned} A_v^w(x) &= 2tan(\theta/2)x \cdot min[max(0, z_c), H] \\ &= 2tan(\theta/2)x \cdot min\left[max\left(0, \frac{B}{x} - \psi_0\right), H\right] \end{aligned} \tag{19}$$

As with Equation (17), this expression holds for all three liquid configurations.

The liquid filled volume for any configuration can be computed by integrating Equation (17) as

$$V^w = \int_0^H A_h^w(z)dz \tag{20}$$

The general result following integration is

$$\begin{aligned} V^w &= tan\left(\frac{\theta}{2}\right)x_L^2 \cdot min[max(0, z_{cL}), H] \\ &+tan\left(\frac{\theta}{2}\right)B^2 \cdot \left[\frac{1}{\psi_0 + min[max(0, z_{cL}), H]} - \frac{1}{\psi_0 + H}\right] \end{aligned} \tag{21}$$

where

$$z_{cL} \equiv \frac{B}{x_L} - \psi_0 \tag{22}$$

The parameter z_{cL} is the liquid height above the baseline at the end of the wedge gap. Combining Equations (9) and (22), Configuration ① corresponds to

Configuration ①:
$$z_{cL} > H \tag{23}$$

and Equation (21) is observed to reduce to Equation (14). Equation (10) for Configuration ② is equivalent to

Configuration ②:
$$0 < z_{cL} < H \tag{24}$$

For Configuration ② Equation (21) simplifies to

$$V^w = tan\left(\frac{\theta}{2}\right) x_L^2 \cdot z_{cL} + tan\left(\frac{\theta}{2}\right) B^2 \cdot \left[\frac{1}{\psi_0 + z_{cL}} - \frac{1}{\psi_0 + H}\right] \tag{25}$$

Configuration ③ corresponds to

Configuration ③:
$$z_{cL} < 0 \tag{26}$$

and Equation (21) simplifies to

$$V^w = tan\left(\frac{\theta}{2}\right) B^2 \cdot \left[\frac{1}{\psi_0} - \frac{1}{\psi_0 + H}\right] \tag{27}$$

Equations (14) , (25) and (27) can also be derived by integrating Equation (19).

Saturation defined by Equation (15) for each of the three liquid configurations, using Equation (13), becomes

Configuration ①:
$$S^w = 1 \tag{28}$$

Configuration ②:
$$S^w = \frac{z_{cL}}{H} + \frac{B^2}{x_L^2 H}\left[\frac{1}{\psi_0 + z_{cL}} - \frac{1}{\psi_0 + H}\right] \tag{29}$$

Configuration ③:
$$S^w = \frac{B^2}{x_L^2 H}\left[\frac{1}{\psi_0} - \frac{1}{\psi_0 + H}\right] \tag{30}$$

These equations define the *water retention* curve for a wedge aperture.

Also of interest for this geometry is the *relative permeability* curve, or equivalently, unsaturated hydraulic conductivity as a function of tension head. A number of investigators have studied wetting and/or drying capillary flow in a parallel plate or wedge geometry (e.g. Sung et al. 2012, Higuera et al. 2008, Barraza et

al. 2002, Siebold et al. 2000, Finn 1999, Schwiebert and Leong 1996). The more rigorous analyses consider inertial and free surface effects on transient flow, such as a non-constant wetting angle. The primary behaviors of interest in this study are: 1) reduced permeability when the air entry pressure is exceeded, and 2) a steep decline in permeability over orders of magnitude as saturation is further reduced towards its residual value. To capture these first-order effects of variable saturation on permeability, and to make the analysis tractable, only viscous and gravitational forces under steady conditions are considered. Furthermore, a parallel plate relationship for permeability is assumed to be locally valid within the wedge geometry, and flow is assumed to be one-dimensional. With these approximations, an effective hydraulic conductivity for the wedge geometry can be derived through spatial integration over the wetted volume as follows.

The hydraulic conductivity for saturated, fully-developed, laminar flow between parallel plates with aperture b is (e.g. Wang and Narasimhan 1985)

$$K = \frac{\rho g b^2}{12\eta} \tag{31}$$

where η = viscosity [N-s/m^2 = kg/m-s]. The viscosity of water at 20°C is 0.00100 N-s/m^2 (Streeter and Wylie 1979, Table C.1). For a fixed vertical hydraulic head gradient of $\lfloor dh/dz \rfloor$ and assuming one-dimensional flow, the total downward flow crossing elevation z based on Darcy's law is

$$Q(z) = \int_0^{min(x_c, x_L)} b(x)K(x)\left|\frac{dh}{dz}\right| dx = \frac{\rho g}{12\eta}\left|\frac{dh}{dz}\right| \int_0^{min(x_c, x_L)} b^3(x)dx \tag{32}$$

The result of integration using Equation (3) is

$$Q(z) = \frac{\rho g}{6\eta}\left|\frac{dh}{dz}\right| tan^3\left(\frac{\theta}{2}\right) min(x_c^4, x_L^4) \tag{33}$$

The effective conductivity at elevation z is define by

$$K_{eff}(z) \equiv \frac{Q(z)}{A_h|dh/dz|} \tag{34}$$

where the horizontal area is

$$A_h = \int_0^{x_L} b(x)dx = tan\left(\frac{\theta}{2}\right)x_L^2 \tag{35}$$

Substituting Equations (33) and (35) into Equation (34) yields

$$K_{eff}(z) = \frac{\rho g}{6\eta} tan^2\left(\frac{\theta}{2}\right)\frac{min(x_c^4, x_L^4)}{x_L^2} \tag{36}$$

The average effective hydraulic conductivity over the height of the finite wedge gap is defined by

$$\overline{K_{eff}} \equiv \frac{\int_0^H K_{eff}(z)dz}{\int_0^H dz} = \frac{1}{H}\frac{\rho g}{6\eta}tan^2\left(\frac{\theta}{2}\right)\frac{1}{x_L^2}\int_0^H min(x_c^4, x_L^4)dz \qquad (37)$$

The integral can be separated into two parts corresponding to fully and partially liquid filled elevations

$$\overline{K_{eff}} = \frac{1}{H}\frac{\rho g}{6\eta}tan^2\left(\frac{\theta}{2}\right)\frac{1}{x_L^2}\left\{\int_0^{min[max(0,z_{cL}),H]} x_L^4 dz + \int_{min[max(0,z_{cL}),H]}^H x_c^4 dz\right\} \qquad (38)$$

Direct integration produces the following result

$$\overline{K_{eff}} = \frac{\rho g\, tan^2(\theta/2)}{6\eta H x_L^2}\left\{x_L^4 \cdot min[max(0,z_{cL}),H]\right.$$
$$\left. + \frac{B^4}{3}\left[\frac{1}{(\psi_0 + min[max(0,z_{cL}),H])^3} - \frac{1}{(\psi_0 + H)^3}\right]\right\} \qquad (39)$$

The expression can be somewhat simplified by introducing

$$b(x_L) = 2tan(\theta/2) \cdot x_L \qquad (40)$$

Equation (39) becomes

$$\overline{K_{eff}} = \frac{1}{2}\frac{\rho g b^2(x_L)}{12\eta}\frac{1}{H}\left\{min[max(0,z_{cL}),H]\right.$$
$$\left. + \frac{1}{3}\left(\frac{B}{x_L}\right)^4\left[\frac{1}{(\psi_0 + min[max(0,z_{cL}),H])^3} - \frac{1}{(\psi_0 + H)^3}\right]\right\} \qquad (41)$$

For Configuration ① ($z_{cL} > H$), Equation (41) reduces to

Configuration ①: $\qquad\qquad \overline{K_{eff}} = \frac{1}{2}\frac{\rho g b^2(x_L)}{12\eta} \qquad (42)$

Equation (42) also represents the saturated conductivity of the wedge gap. For Configuration ② ($0 < z_{cL} < H$), Equation (41) become

Configuration ②: $\quad \overline{K_{eff}} = \frac{1}{2}\frac{\rho g b^2(x_L)}{12\eta}\frac{1}{H}\left\{z_{cL} + \frac{1}{3}\left(\frac{B}{x_L}\right)^4\left[\frac{1}{(\psi_0 + z_{cL})^3} - \frac{1}{(\psi_0 + H)^3}\right]\right\} \quad (43)$

For Configuration ③ ($z_{cL} < 0$), Equation (41) simplifies to

Configuration ③: $\quad \overline{K_{eff}} = \frac{1}{2}\frac{\rho g b^2(x_L)}{12\eta}\frac{1}{H}\left\{\frac{1}{3}\left(\frac{B}{x_L}\right)^4\left[\frac{1}{(\psi_0)^3} - \frac{1}{(\psi_0 + H)^3}\right]\right\} \quad (44)$

11

Relative permeabilities corresponding to Equations (42) through (44) are summarized as

$$Configuration\ ①: \qquad\qquad k_r = 1 \qquad\qquad (45)$$

$$Configuration\ ②: \qquad k_r = \frac{1}{H}\left\{z_{cL} + \frac{1}{3}\left(\frac{B}{x_L}\right)^4\left[\frac{1}{(\psi_0 + z_{cL})^3} - \frac{1}{(\psi_0 + H)^3}\right]\right\} \qquad (46)$$

$$Configuration\ ③: \qquad k_r = \frac{1}{H}\left\{\frac{1}{3}\left(\frac{B}{x_L}\right)^4\left[\frac{1}{(\psi_0)^3} - \frac{1}{(\psi_0 + H)^3}\right]\right\} \qquad (47)$$

Table 2-1 summarizes the key results derived above for a wedge-shaped aperture in terms of the three specific liquid configurations.

The general result for saturation, valid for all three liquid configurations, is the quotient of Equation (21) and (13), respectively. The result is

$$S^w = \frac{1}{H}min[max(0, z_{cL}), H] + \frac{B^2}{x_L^2 H}\left[\frac{1}{\psi_0 + min[max(0, z_{cL}), H]} - \frac{1}{\psi_0 + H}\right] \qquad (48)$$

Similarly, a general result for relative permeability can be derived from Equation (41) by dividing by Equation (42)

$$k_r = \frac{1}{H}\left\{min[max(0, z_{cL}), H]\right.$$
$$\left. + \frac{1}{3}\left(\frac{B}{x_L}\right)^4\left[\frac{1}{(\psi_0 + min[max(0, z_{cL}), H])^3} - \frac{1}{(\psi_0 + H)^3}\right]\right\} \qquad (49)$$

The general results are summarized in Table 2-2.

Table 2-3 defines specific parameters values for a wedge aperture for the purpose of plotting an example hydraulic conductivity curve. The "number of apertures" and "volume of apertures" in the table are defined in anticipation of experimental testing to be described in the next section, and do not affect hydraulic conductivity. Figure 2-3 illustrates the hydraulic conductivity curve corresponding to Table 2-3. The air-entry pressure head is 21.55 cm and the relative permeability is 1.0 for tension heads less than this value. Beyond ψ_0 = 21.55 cm, hydraulic conductivity declines sharply. The transition between Configurations ① and ③ is small, occurring over a tension head range of only H = 2.5 cm.

Table 2-1. Summary of hydraulic properties derived for a wedge-shaped aperture for specific conditions.

Definitions

$$B = \frac{\sigma \cos(\varphi)}{\rho g \tan(\theta/2)} \qquad z_{cL} = \frac{B}{x_L} - \psi_0 \qquad b(x_L) = 2\tan(\theta/2) \cdot x_L$$

Configuration ①

$$\psi_0 < \frac{B}{x_L} - H \qquad \text{or equivalently} \qquad z_{cL} > H$$

$$S^w = 1$$

$$\overline{K_{eff}} = \frac{1}{2}\frac{\rho g b^2(x_L)}{12\eta}$$

$$k_r = 1$$

Configuration ②

$$\frac{B}{x_L} - H < \psi_0 < \frac{B}{x_L} \qquad \text{or equivalently} \qquad 0 < z_{cL} < H$$

$$S^w = \frac{z_{cL}}{H} + \frac{B^2}{x_L^2 H}\left[\frac{1}{\psi_0 + z_{cL}} - \frac{1}{\psi_0 + H}\right]$$

$$\overline{K_{eff}} = \frac{1}{2}\frac{\rho g b^2(x_L)}{12\eta}\frac{1}{H}\left\{z_{cL} + \frac{1}{3}\left(\frac{B}{x_L}\right)^4\left[\frac{1}{(\psi_0 + z_{cL})^3} - \frac{1}{(\psi_0 + H)^3}\right]\right\}$$

$$k_r = \frac{1}{H}\left\{z_{cL} + \frac{1}{3}\left(\frac{B}{x_L}\right)^4\left[\frac{1}{(\psi_0 + z_{cL})^3} - \frac{1}{(\psi_0 + H)^3}\right]\right\}$$

Configuration ③

$$\psi_0 > \frac{B}{x_L} \qquad \text{or equivalently} \qquad z_{cL} < 0$$

$$S^w = \frac{B^2}{x_L^2 H}\left[\frac{1}{\psi_0} - \frac{1}{\psi_0 + H}\right]$$

$$\overline{K_{eff}} = \frac{1}{2}\frac{\rho g b^2(x_L)}{12\eta}\frac{1}{H}\left\{\frac{1}{3}\left(\frac{B}{x_L}\right)^4\left[\frac{1}{(\psi_0)^3} - \frac{1}{(\psi_0 + H)^3}\right]\right\}$$

$$k_r = \frac{1}{H}\left\{\frac{1}{3}\left(\frac{B}{x_L}\right)^4\left[\frac{1}{(\psi_0)^3} - \frac{1}{(\psi_0 + H)^3}\right]\right\}$$

Table 2-2. Summary of hydraulic properties derived for a wedge-shaped aperture for general conditions.

<table>
<tr><td colspan="3" align="center">Definitions</td></tr>
<tr>
<td>$B = \frac{\sigma cos(\varphi)}{\rho g tan(\theta/2)}$</td>
<td>$z_{cL} = \frac{B}{x_L} - \psi_0$</td>
<td>$b(x_L) = 2 tan(\theta/2) \cdot x_L$</td>
</tr>
</table>

<table>
<tr><td align="center">All Configurations</td></tr>
<tr><td>

$$S^w = \frac{1}{H} min[max(0, z_{cL}), H] + \frac{B^2}{x_L^2 H}\left[\frac{1}{\psi_0 + min[max(0, z_{cL}), H]} - \frac{1}{\psi_0 + H}\right]$$

$$\overline{K_{eff}} = \frac{1}{2}\frac{\rho g b^2(x_L)}{12\eta}\frac{1}{H}\left\{min[max(0, z_{cL}), H] + \frac{1}{3}\left(\frac{B}{x_L}\right)^4\left[\frac{1}{(\psi_0 + min[max(0, z_{cL}), H])^3} - \frac{1}{(\psi_0 + H)^3}\right]\right\}$$

$$k_r = \frac{1}{H}\left\{min[max(0, z_{cL}), H] + \frac{1}{3}\left(\frac{B}{x_L}\right)^4\left[\frac{1}{(\psi_0 + min[max(0, z_{cL}), H])^3} - \frac{1}{(\psi_0 + H)^3}\right]\right\}$$

</td></tr>
</table>

Table 2-3. Parameters values for example wedge geometry.

Parameter	Symbol	Value	Units
Gravitational acceleration	g	9.81	m/s^2
Liquid density	ρ	998	kg/m^3
Viscosity	η	0.001002	kg/m-s
Surface tension	σ	0.07275	N/m
Contact angle	φ	**25**	deg
		0.436	rad
Plate length	L	0.05	m
		5	cm
End spacing	b_L	0.000056	m
		0.056	mm
		2.20	mil
Separation angle	θ	0.00112	rad
		0.064	deg
	tan(θ/2)	0.00056	
	cos(θ/2)	0.9999998	
Gap length	x_L=Lcos(θ/2)	0.05	m
Flach grouping	B	0.012026	m^2
Sample height	H	0.025	m
		2.5	cm
Volume of aperture	V	3.5E-08	m^3
		0.035	mL
Number of apertures	N	50	
Volume of apertures	NV	1.75E-06	m^3
		1.7499997	mL
Configuration ①→②	B/x_L - H	0.2155	m
transition	(air entry ψ)	**21.55**	**cm**
Configuration ②→③	B/x_L	0.2405	m
transition		24.05	cm
	b(x_L)	0.000056	m
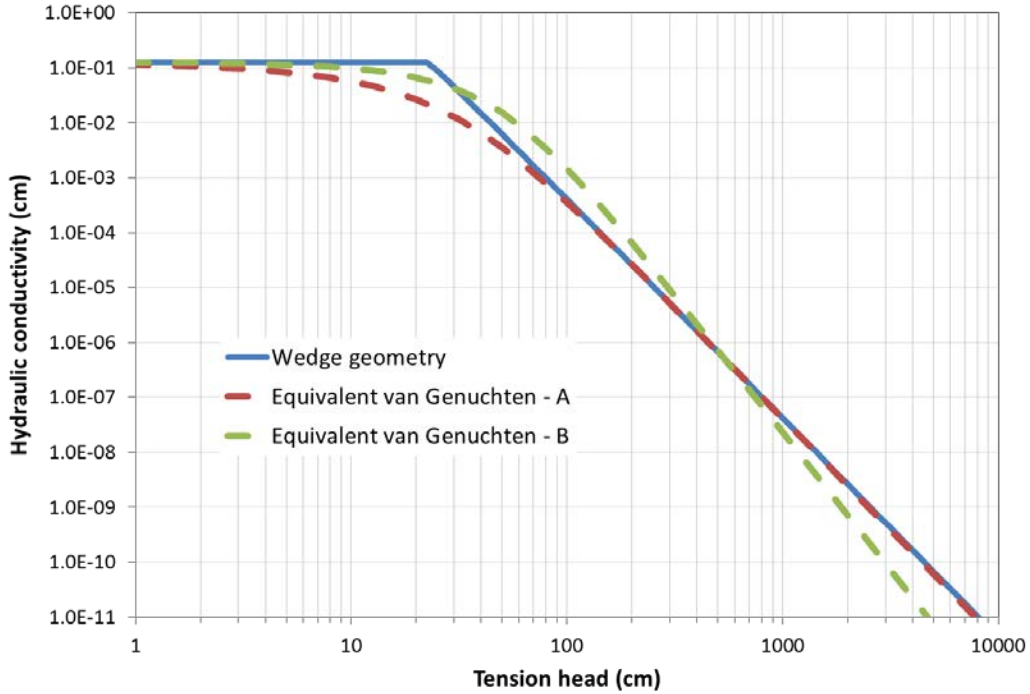
Figure 2-3. Example hydraulic conductivity curves for a wedge geometry and two approximating van Genuchten (1980) / Mualem (1976) curves.

Also shown in Figure 2-3 are two somewhat equilvalent van Genuchten (1980) / Mualem (1976) (vGM) curves that approximate the analytic wedge solution in two manners. By design both curves match the saturated conductivity of the analytic solution (through specification of the same K_s). The vGM function forms are defined as follows. An effective saturation S_e is defined in terms of water content Θ, or equivalently saturation S, as

$$S_e \equiv \frac{\Theta - \Theta_r}{\Theta_s - \Theta_r} = \frac{S - S_r}{1 - S_r} \tag{50}$$

where the subscripts refer to saturated (s) and residual (r) conditions. The van Genuchten (1980) functional form for effective saturation is

$$S_e = \frac{1}{[1 + (\alpha\psi)^n]^m} \tag{51}$$

The Mualem (1976) assumption is

$$m = 1 - \frac{1}{n} \tag{52}$$

The functional form for relative permeability is

$$k_r = S_e^{1/2} \left[1 - \left(1 - S_e^{1/m} \right)^m \right]^2 \qquad (53)$$

With consideration of Equation (52) the independent parameters are α and n. The parameter α controls the air-entry pressure and n controls the slope of conductivity versus tension head in the unsaturated region.

The vGM functional forms were developed for soils and are not necessarily expected to be suitable for representing drainage from a wedge-shaped fracture, hence approximation can be anticipated. Indeed, the vGM functional form exhibits a smoother transition between saturated and unsaturated conditions than the analytic wedge solution. vGM curve A is designed to match the analytic solution at high tension heads. vGM curve B is designed to more closely approximate the analytic solution at intermediate suctions heads between 10 and 100 cm. Table 2-4 defines the independent vGM parameters for the two approximations.

Table 2-4. Parameter values for van Genuchten / Mualem curves approximating the wedge analytic solution.

Parameter	vGM curve A	vGM curve B	Units
α	0.027	0.0175	1/cm
n	1.82	2.2	-

3.0 Method Validation Specimen

Leveraging the analytic results summarized in Table 2-1 and Table 2-2 for a single wedge aperture, a synthetic medium with multiple fractures was constructed for experimental method validation by assembling microscope slides that had been trimmed in length to a nominal length of 5 cm. Standard adhesive tape was applied to one end of each slide to create a wedge-shaped aperture between adjacent slides. A total of 51 slides were arranged to form a trapezoidal shaped block with 50 wedge shaped apertures (Figure 3-1). The legs of the trapezoidal block were 5.194 cm and 4.915 cm in width with a length of 5.080 cm and height of 2.500 cm. The block assemblage was held together with two rubber bands. The total fracture volume of the block was calculated to be 1.75 mL and the estimated porosity was 0.0276. The average shim (adhesive tape) thickness was calculated at 0.056 mm. The glass slides were washed with soap, rinsed with deionized water, and dried with a lint-free towel. The wetting/contact angle was not measured and presumed to be on the order of 25 degrees. This setting and the other parameter values in Table 2-3 apply to the glass plate assemblage.
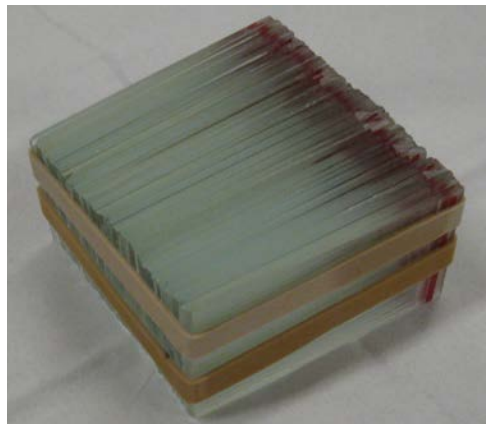
Figure 3-1. Assemblage of microscope slides used as fractured medium analog.

4.0 Experimental Apparatus and Procedure

Dixon and Nichols (2013) describe the experimental apparatus and procedure used previously to test fractured grout samples, and note some of the complications in using the method to investigate the hydraulic properties of fractured media. The same method and apparatus were used to test the block of glass microscope slides. For completeness a brief description of the apparatus and test method are included herein.

The outflow extraction system consists of the outflow extractor, a peristaltic pump, and a high precision balance to monitor effluent from the extractor (Figure 4-1). The outflow extractor contains a porous ceramic that provides the interface between the applied pressure inside the extractor and ambient atmospheric pressure outside the extractor. The sample rests inside the extractor on the surface of the porous ceramic plate. For the purposes of this testing, a high flow porous ceramic plate with an air entry pressure of 1000 cm H2O was selected. The saturated hydraulic conductivity of the plate is reported by the manufacturer (Soil Moisture, Inc.) to be 8.6E-06 cm/s. Prior to the start of each test, the plate was saturated with de-aired water. This was accomplished by pressurizing a known mass of de-aired water in the chamber. This allowed the de-aired water to flow through the plate until the chamber was empty thereby saturating the plate. Care was taken not to exceed the air entry pressure of the plate during this process. Outflow was monitored on the digital balance to determine when the bulk of the water had been pushed through the plate.

Figure 4-1. Outflow extractor, fraction collector, peristaltic pump, and high precision digital balance used in transient outflow extraction tests.

The outflow extractor consists of a single inlet port for pressure application. The outlet side of the extractor consists of two ports, one which is used to drain effluent from the sample and a secondary port that is used to remove air from beneath the ceramic plate prior to testing. Using an arrangement of valves, the two outlet ports, and a peristaltic pump, de-aired water was circulated beneath the ceramic plate to remove entrapped air. Once this process was completed, a valve was used to close the secondary outlet port. Small diameter tubing was connected to the primary outlet port. The end of this tubing was maintained at a height equal to the bottom of the sample. Outflow experiments were carried out by

pressurizing the extractor using compressed air. Several pressure increments were used in each transient test ranging from about 5 to 100 cm H$_2$O. These pressures were maintained using a series of high precision multistage gas regulators. Effluent from each sample was monitored using a digital balance and logged directly to a computer every five seconds. Ultimately, the balance served as a drop counter and the mass of each drop of water was converted to volume using a density of 1.00 g/cm^3. Cumulative outflow was converted to cumulative flux by dividing the volume of effluent by the total area of the sample.

As measured by the effluent mass balance, the volume of water extracted during the three tests was 1.79, 1.71 and 1.74 mL for an average of 1.75 mL, compared to a computed void volume of 1.75 mL. Following the Test02 and Test04 outflow tests, the sample was removed from the ceramic plate and weighed to determine the total mass of water removed from the block of slides by a second means. The volume computed by this method was 2.03 and 2.04 g, which averages 18% larger than the two Test02 and Test04 effluent mass balance readings.

5.0 Experimental Method Validation

In the Multistep Outflow Method, van Genuchten / Mualem parameters are estimated from cumulative outflow data through inverse modeling. The HYDRUS-1D code (Šimůnek et al. 2008) was chosen for data fitting in this study. One-dimensional analysis was performed with the recognition that the predominant flow is downward; lateral flow is assumed to be minimal.

The matrix, being composed of (solid) glass, contributes nothing to the flow extracted from the validation specimen under increasing gas pressure. As a result the matrix may be included or excluded from the inverse modeling estimation of vGM parameters (α, n); that is, analyses of the matrix and fractures together or just the fractures are mathematically equivalent. The reason is that effective saturation on a total (matrix + fracture) area basis S_e is identical to effective saturation in a fracture area basis S_{fe}

$$S_e = \frac{\Theta - \Theta_r}{\Theta_s - \Theta_r} = \frac{\Theta_f - \Theta_{fr}}{\Theta_{fs} - \Theta_{fr}} = S_{fe} \qquad (54)$$

More generally, this relationship holds for a matrix that is porous provided its water content does not change over the range of pressure heads tested.

For a matrix+fracture analysis, volumetric liquid flux is naturally based on the total area of the tested specimen and the conductivity assigned to the porous ceramic pressure plate supporting the fractured medium is that measured for the material (K_{plate} = 8.6E-06 cm/s). For a fracture-only analysis, volumetric flux is based on the fracture area; however, the conductivity of the plate must be modified in a 1D inverse analysis to account for 2D spreading of flow beneath the specimen. Because the flow through the ceramic pressure plate will spread across the entire area beneath the fracture medium, the conductivity adjustment should be adjusted as

$$K_{plate}^{adjusted} = \frac{A_{total}}{A_{fracture}} K_{plate} \qquad (55)$$

to reflect two-dimensional flow that effectively increases the transmissivity of the layer.

HYDRUS-1D is a finite-element flow simulator such that material properties are defined at element faces and material boundaries implicitly occur between element faces. Figure 5-1 illustrates the finite-element grid selected for inverse modeling. The grid is composed of 15 elements residing completely within the

test specimen, 5 elements within the pressure plate, and a transition element straddling the material interface, for a total of 21 elements. Using a modest number of elements improved the robustness of inverse modeling compared to using larger numbers on the order of 100 elements.
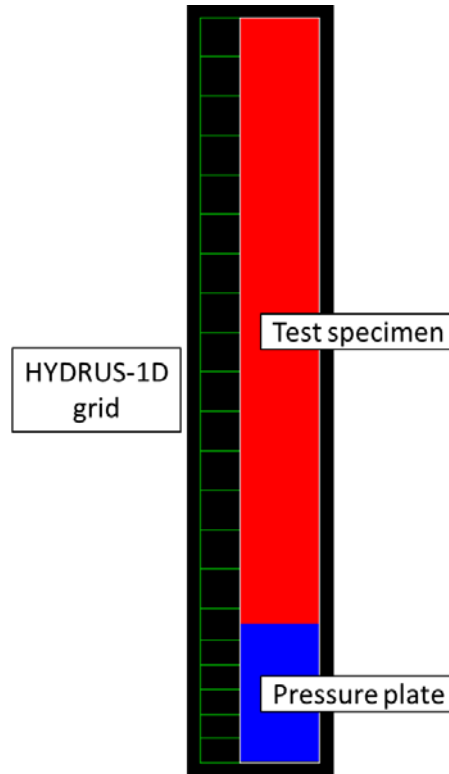
Figure 5-1. Grid selected for HYDRUS-1D inverse modeling.

Element sizes must be carefully selected to achieve the desired position of the material interface. For n_i elements in region i of height H_i and n_j elements in region j of height H_j, the proper element size in region i can be shown through algebraic manipulation to be

$$\Delta z_i = \frac{4H_i(4n_j + 1) - 4H_j}{(4n_i + 1)(4n_j + 1) - 1} \tag{56}$$

The element size in the other region is gotten by swapping indices. The middle element size is the average of the surrounding element sizes

$$\Delta z_{i+j} = 0.5(\Delta z_i + \Delta z_j) \tag{57}$$

Three experiments were completed using the same glass plate specimen described above: Test01, Test02 and Test04 (Test03 was aborted). Appendix A provides the detailed experimental data acquired for HYDRUS-1D inverse modeling. A matrix of four inverse modeling parameter fits were conducted for each set of test data, as indicated in Table 5-1 through Table 5-3, part (a). Residual conditions were apparently achieved by the end of test and the cumulative volume of liquid extracted was approximately

equal to the computed void volume based on overall dimensions of the assembled test specimen. Therefore, the residual water content / saturation is set to zero for inverse modeling. For inverse fit Fit01, the saturated hydraulic conductivity is fixed at the analytic value given by Equation (42):

$$K_s = \frac{1}{2}\frac{\rho g b^2(x_L)}{12\eta} \tag{58}$$

For Fit03 K_s is scaled downward by the ratio of fracture area to total area. For cases Fit02 and Fit04 K_s is a fitted parameter. For cases Fit01 and Fit02, only the fracture area is considered in defining cumulative water flux, whereas for Fit03 and Fit04 the total area is assumed to be available for flow. For the Test04 data, the van Genuchten n parameter became practically unbounded (excessively large) and was subsequently constrained to be ≤ 8.0 for Fit02 and Fit04, and then ≤ 6.0 for Fit02b and Fit04b.

Figure 5-2 through Figure 5-4 compare the measured and simulated cumulative liquid flux extracted through time. The inverse fitting results for Fit01 and Fit03, and Fit02 and Fit04, shown in parts (b) of Table 5-1 through Table 5-3, are observed to be practically the same, confirming the earlier assertion that choice of a fracture or total area viewpoint is arbitrary. Table 5-4 summarizes the individual inverse fitting results and presents average values across the three experimental data sets. For inverse modeling where n was constrained, the fitting results for $n \leq 6$ were selected for averaging. Fitted values of K_s are significantly smaller than the expected values based on Equation (58). Table 5-5 shows the vGM parameters from Table 2-4 in a form more suitable for comparison to part (b) of Table 5-1 through Table 5-3. Fitted values of α are significantly larger than α values for the vGM curves approximating the analytic solution, indicating a much lower air-entry pressure than expected. Fitted values of n are higher than expected from the approximating vGM curves, indicating a steeper decline in conductivity in the unsaturated region.

Parts (c) of Table 5-1 through Table 5-3 show the correlation matrices for the parameters estimated through inverse modeling. Correlation values approaching ±1.0 indicate strong parameter correlation and highly uncertain or practically non-unique parameter estimates. Values around 0.0 indicate low correlation and unique parameter estimates. None of the correlation coefficients in parts (c) of Table 5-1 through Table 5-3 are near ±1.0, suggesting that unique fits have been attained through inverse modeling. Notwithstanding inherent tendencies for non-uniqueness in inverse modeling, this outcome is not unexpected, considering that the parameters K_s (Test02 and Test04 only), α and n control different attributes of the hydraulic conductivity curve.

Figure 5-5 compares the vGM curves derived through inverse modeling with α and n variable to the analytic curve derived for a wedge fracture. Figure 5-6 provides a similar comparison for the case of α, n and K_s as the fitted parameters. Also shown in these plots is an "effective plate conductivity" defined as

$$K_p^{eff} = H_s/H_p \cdot K_p \tag{59}$$

where H_s and H_p are the heights of the specimen and pressure plate, respectively. Comparing K_s and K_p^{eff} is equivalent to comparing the leakances of the two regions (conductivity divided by region thickness). The pressure plate is observed to be the most significant resistance to overall flow until the tension head exceeds roughly 10 cm. This characteristic of the test apparatus makes estimation of the saturated conductivity particularly uncertain. Figure 5-6 indicates a fitted conductivity that is one and half orders of magnitude smaller than expected. The discrepancy could be a result of the pressure plate being excessive resistive and masking the test specimen at low applied gas pressures, although this possibility has not been demonstrated.

21

Table 5-1. Inverse modeling matrix and results – Test01.

(a) Inverse modeling matrix

Case	θ_r	θ_s	α	n	K_s (cm/s)	K_s (cm/h)	$\Delta\theta$	Comment
Fit01	0	1	fitted	fitted	1.28E-01	459.62023	1.000	Fracture
Fit02	0	1	fitted	fitted	fitted	fitted	1.000	Fracture
Fit03	0	0.0276	fitted	fitted	3.52E-03	12.685518	0.028	Fracture + Matrix
Fit04	0	0.0276	fitted	fitted	fitted	fitted	0.028	Fracture + Matrix

(b) Inverse modeling parameter results

Case	θ_r	θ_s	α	n	K_s (cm/s)	K_s (cm/h)	R2	Comment
Fit01	0	1	0.085	3.39	1.28E-01	459.62023	0.940	GlassPlates_Test04.h1d
Fit02	0	1	0.092	4.15	1.54E-03	5.5613	0.992	GlassPlates_Test04b.h1d
Fit03	0	0.0276	0.086	3.40	3.52E-03	12.685518	0.941	GlassPlates_Test04c.h1d
Fit04	0	0.0276	0.092	4.20	4.24E-05	0.15274	0.992	GlassPlates_Test04d.h1d

(c) Inverse modeling correlation matrices

Fit01	alpha	n		**Fit03**	alpha	n	
alpha	1			alpha	1		
n	-0.7431	1		n	-0.7432	1	
Fit02	alpha	n	Ks	**Fit04**	alpha	n	Ks
alpha	1			alpha	1		
n	-0.7882	1		n	-0.795	1	
Ks	-0.3875	0.0242	1	Ks	-0.3373	-0.0409	1
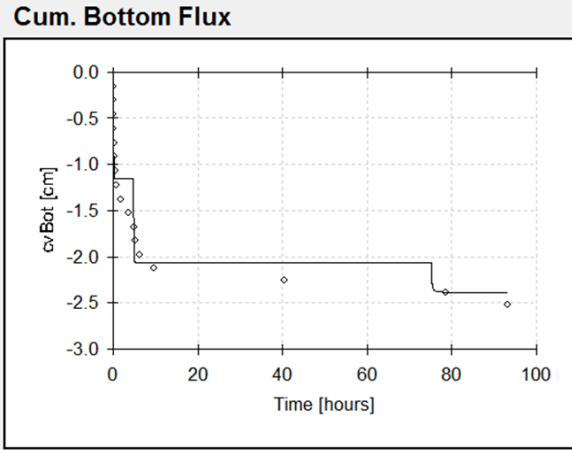
(a) Fit01
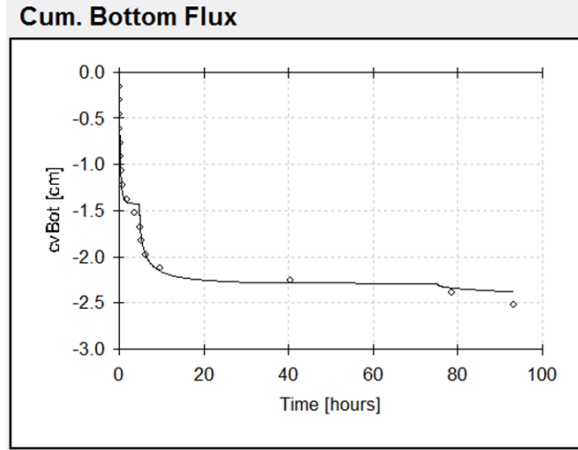
(b) Fit02
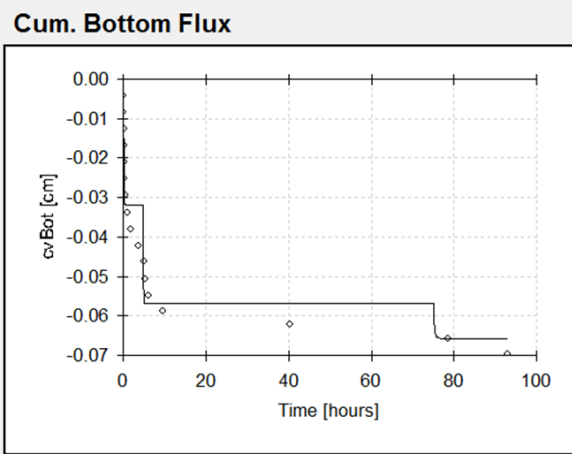
(c) Fit03
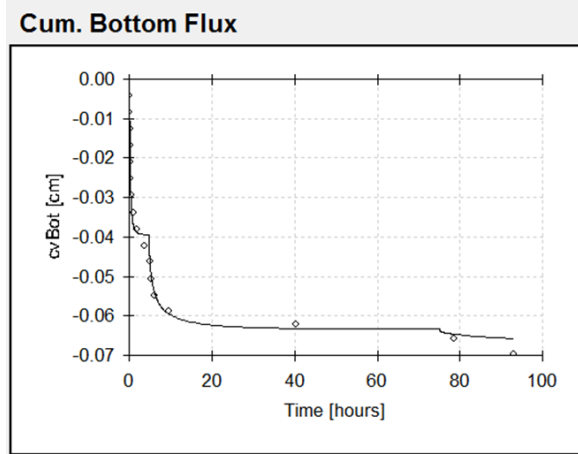
(d) Fit04

○ = measured data   — = model simulation

Figure 5-2. Measured and simulated cumulative liquid flux – Test01.

Table 5-2. Inverse modeling matrix and results – Test02.

(a) Inverse modeling matrix

Case	θ_r	θ_s	α	n	K_s (cm/s)	K_s (cm/h)	$\Delta\theta$	Comment
Fit01	0	1	fitted	fitted	1.28E-01	459.62023	1.000	Fracture
Fit02	0	1	fitted	fitted	fitted	fitted	1.000	Fracture
Fit03	0	0.0276	fitted	fitted	3.52E-03	12.685518	0.028	Fracture + Matrix
Fit04	0	0.0276	fitted	fitted	fitted	fitted	0.028	Fracture + Matrix

(b) Inverse modeling parameter results

Case	θ_r	θ_s	α	n	K_s (cm/s)	K_s (cm/h)	R2	Comment
Fit01	0	1	0.109	2.67	1.28E-01	459.62023	0.912	GlassPlates_Test04.h1d
Fit02	0	1	0.106	3.27	4.15E-03	1.49E+01	0.957	GlassPlates_Test04b.h1d
Fit03	0	0.0276	0.108	2.71	3.52E-03	12.685518	0.912	GlassPlates_Test04c.h1d
Fit04	0	0.0276	0.105	3.31	1.13E-04	0.40573	0.958	GlassPlates_Test04d.h1d

(c) Inverse modeling correlation matrices

Fit01	alpha	n		Fit03	alpha	n	
alpha	1			alpha	1		
n	-0.8081	1		n	-0.8008	1	
Fit02	alpha	n	Ks	**Fit04**	alpha	n	Ks
alpha	1			alpha	1		
n	-0.6131	1		n	-0.605	1	
Ks	0.0925	-0.5973	1	Ks	0.0638	-0.5684	1
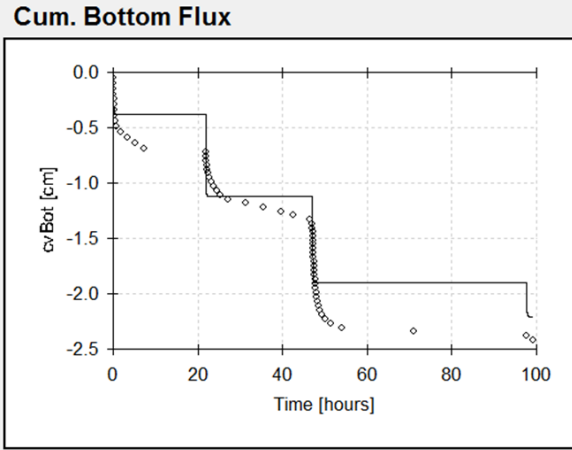
(a) Fit01
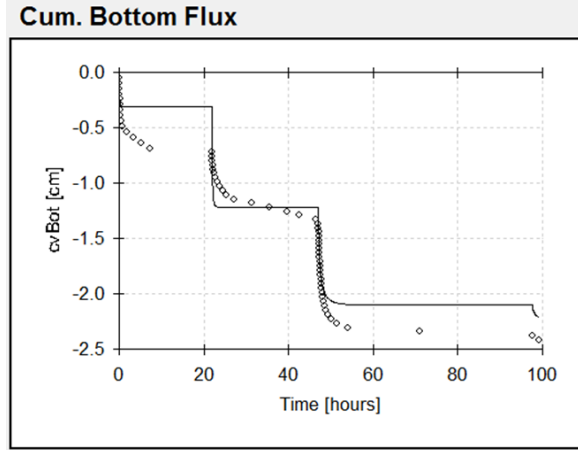
(b) Fit02
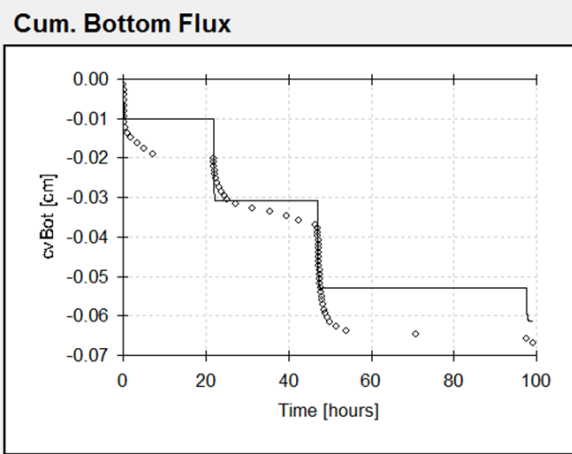
(c) Fit03
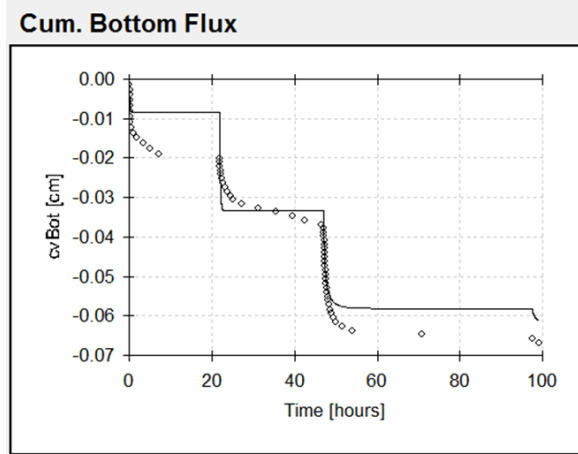
(d) Fit04

○ = measured data   — = model simulation

Figure 5-3. Measured and simulated cumulative liquid flux – Test02.

Table 5-3. Inverse modeling matrix and results – Test04.

(a) Inverse modeling matrix

Case	θ_r	θ_s	α	n	K_s (cm/s)	K_s (cm/h)	$\Delta\theta$	Comment
Fit01	0	1	fitted	fitted	1.28E-01	459.62023	1.000	Fracture
Fit02	0	1	fitted	fitted	fitted	fitted	1.000	Fracture
Fit03	0	0.0276	fitted	fitted	3.52E-03	12.685518	0.028	Fracture + Matrix
Fit04	0	0.0276	fitted	fitted	fitted	fitted	0.028	Fracture + Matrix

(b) Inverse modeling parameter results

Case	θ_r	θ_s	α	n	K_s (cm/s)	K_s (cm/h)	R2	Comment
Fit01	0	1	0.077	4.41	1.28E-01	459.62023	0.865	GlassPlates_Test04.h1d
Fit02	0	1	0.078	8.00*	1.99E-03	7.1505	0.914	GlassPlates_Test04b.h1d
Fit02b	0	1	0.078	6.00*	2.41E-03	8.6863	0.909	GlassPlates_Test04bb.h1d
Fit03	0	0.0276	0.077	4.43	3.52E-03	12.685518	0.865	GlassPlates_Test04c.h1d
Fit04	0	0.0276	0.078	8.00*	6.75E-05	0.24304	0.913	GlassPlates_Test04d.h1d
Fit04b	0	0.0276	0.078	6.00*	1.20E-04	0.43059	0.905	GlassPlates_Test04dd.h1d

* constrained value

(c) Inverse modeling correlation matrices

Fit01	alpha	n		**Fit03**	alpha	n	
alpha	1			alpha	1		
n	-0.4836	1		n	-0.4839	1	
Fit02	alpha	n	Ks	**Fit04**	alpha	n	Ks
alpha	1			alpha	1		
n	-0.0872	1		n	-0.0673	1	
Ks	-0.1786	-0.5705	1	Ks	-0.2029	-0.5837	1
Fit02b	alpha	n	Ks	**Fit04b**	alpha	n	Ks
alpha	1			alpha	1		
n	-0.2142	1		n	-0.2599	1	
Ks	-0.0657	-0.6148	1	Ks	-0.0017	-0.613	1
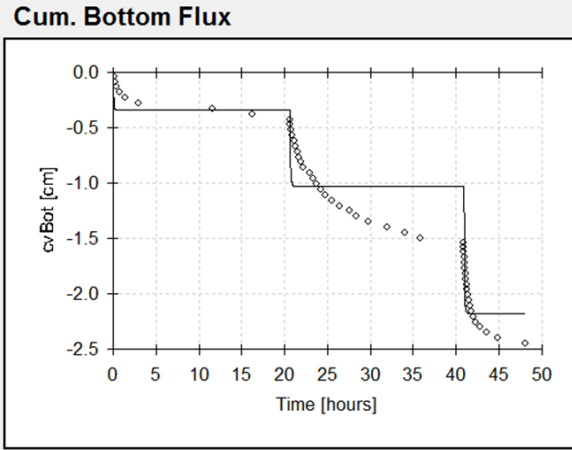
(a) Fit01
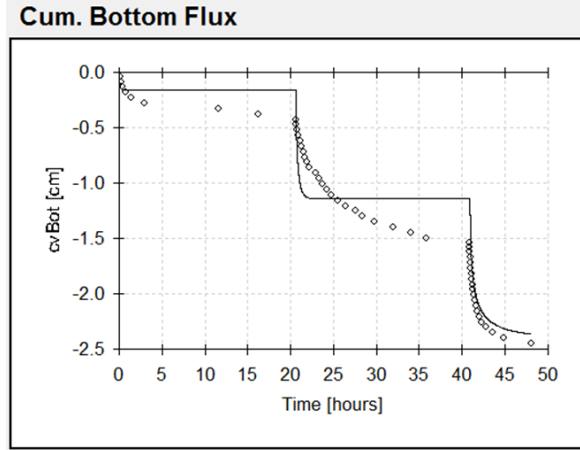
(b) Fit02
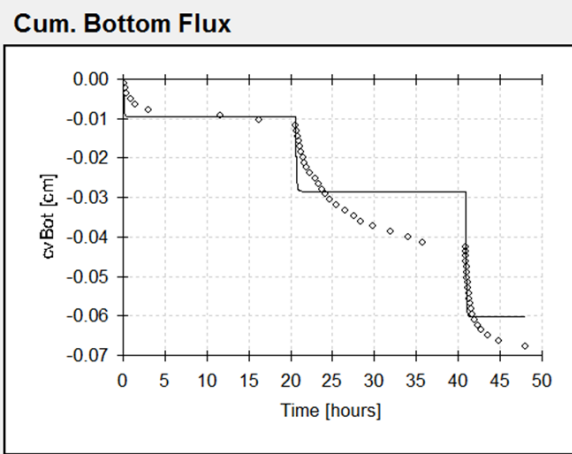
(c) Fit03
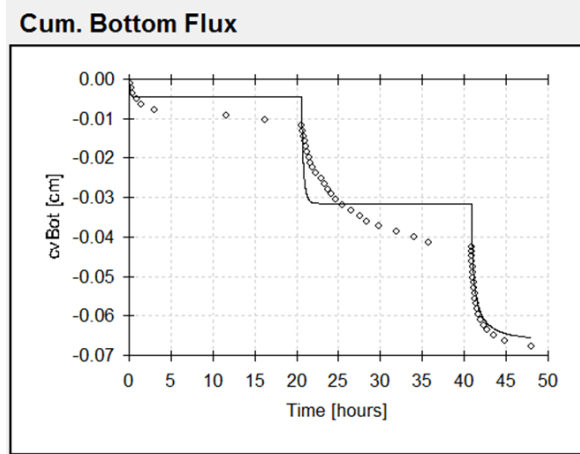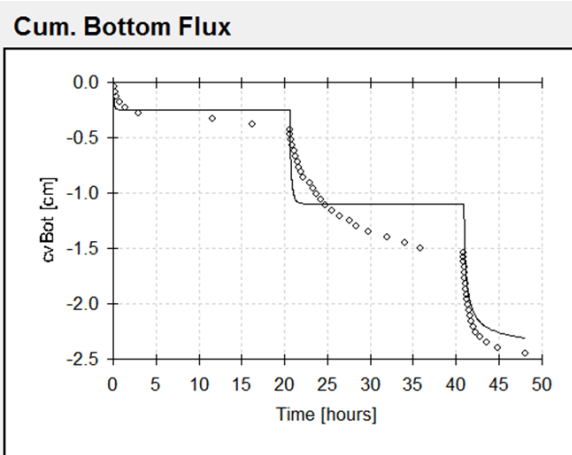
(d) Fit04

(e) Fit02b
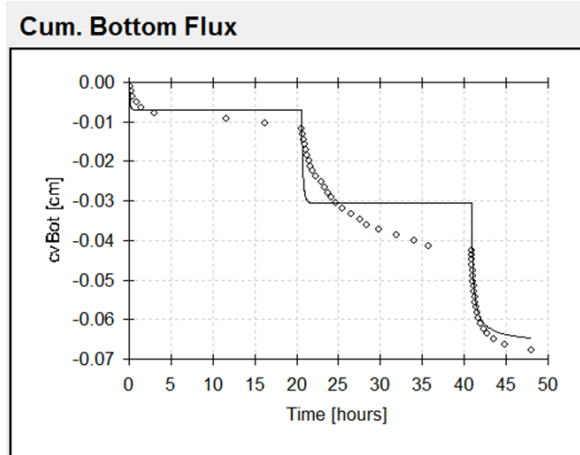
(f) Fit04b

○ = measured data   — = model simulation

Figure 5-4. Measured and simulated cumulative liquid flux – Test04.

Table 5-4. Average and individual test results from HYDRUS-1D inverse modeling.

Case, Test	θ_r	θ_s	α (1/cm)	n	K_s fracture (cm/s)	K_s total (cm/s)	Comment
	fixed	fixed	fitted	fitted	fixed	calculated	Compared to analytic solution
Fit01	**0**	**1**	**0.091**	**3.5**	**1.3E-01**	**3.5E-03**	surrogate vG function:
Test01			0.085	3.4	1.3E-01	3.5E-03	higher α (lower air entry pressure)
Test02			0.109	2.7	1.3E-01	3.5E-03	higher n (steeper down slope)
Test04			0.077	4.4	1.3E-01	3.5E-03	same K_s (by choice)
	fixed	fixed	fitted	fitted	fitted	calculated	Compared to Fit01 (α, n fit):
Fit02	**0**	**1**	**0.092**	**4.5**	**2.7E-03**	**7.5E-05**	same α (same air entry pressure)
Test01			0.092	4.2	1.5E-03	4.3E-05	higher n (steeper down slope)
Test02			0.106	3.3	4.1E-03	1.1E-04	lower K_s (slower response)
Test04		wt	0.078	6.0*	2.4E-03	6.7E-05	
4a		0	0.078	8.0*	2.0E-03	5.5E-05	
4b		1	0.078	6.0*	2.4E-03	6.7E-05	
	fixed	fixed	fitted	fitted	calculated	fixed	Compared to Fit01 (fracture area fit):
Fit03	**0**	**0.0276**	**0.090**	**3.5**	**1.3E-01**	**3.5E-03**	parameters same as Fit01
Test01			0.086	3.4	1.3E-01	3.5E-03	parameters same as Fit01
Test02			0.108	2.7	1.3E-01	3.5E-03	parameters same as Fit01
Test04			0.077	4.4	1.3E-01	3.5E-03	parameters same as Fit01
	fixed	fixed	fitted	fitted	calculated	fitted	Compared to Fit02 (fracture area fit):
Fit04	**0**	**0.0276**	**0.092**	**4.5**	**3.3E-03**	**9.2E-05**	parameters ~same as Fit02
Test01			0.092	4.2	1.5E-03	4.2E-05	parameters same as Fit02
Test02			0.105	3.3	4.1E-03	1.1E-04	parameters same as Fit02
Test04		wt	0.078	6.0*	4.3E-03	1.2E-04	parameters ~same as Fit02
4a		0	0.078	8.0*	2.4E-03	6.8E-05	parameters ~same as Fit02
4b		1	0.078	6.0*	4.3E-03	1.2E-04	parameters ~same as Fit02

Table 5-5. van Genuchten parameters approximating the analytic wedge fracture solution.

Material	θ_r	θ_s	α (1/cm)	n	K_s (cm/s)	K_s (cm/h)	$\Delta\theta$	Comment
Surrogate.a	0	1	0.027	1.82	1.28E-01	459.62023	1.000	Fracture
Surrogate.b	0	1	0.0175	2.2	1.28E-01	459.62023	1.000	Fracture
Surrogate.c	0	0.0276	0.027	1.82	3.52E-03	12.685518	0.028	Fracture + Matrix
Surrogate.d	0	0.0276	0.0175	2.2	3.52E-03	12.685518	0.028	Fracture + Matrix
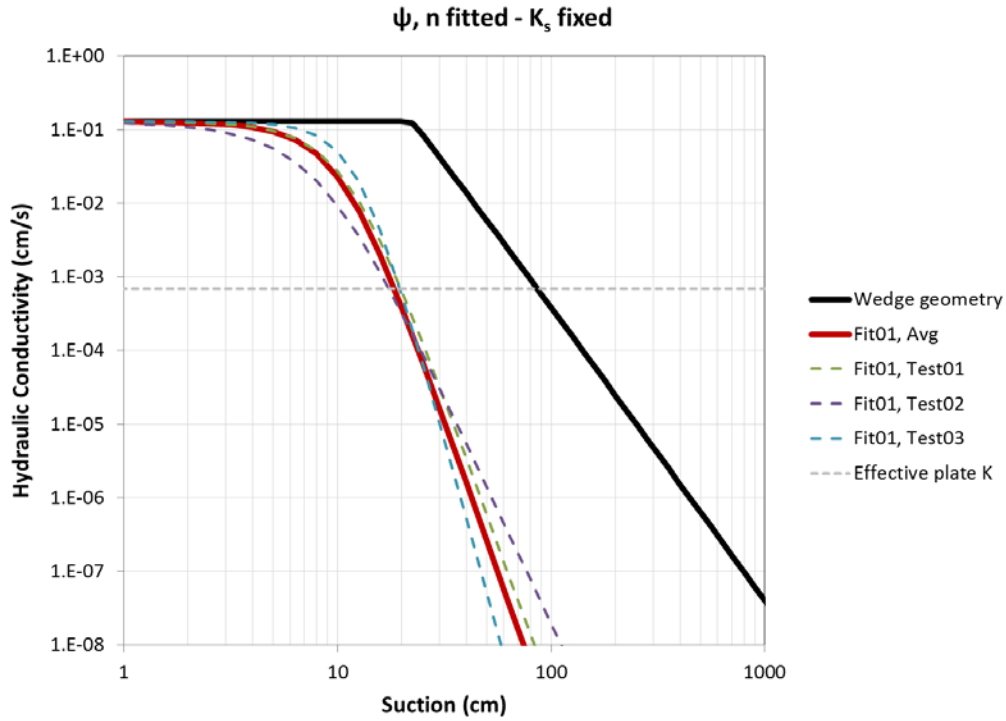
Figure 5-5. Inverse modeling fits compared to analytic wedge fracture solution – α and n fitted, K_s fixed.
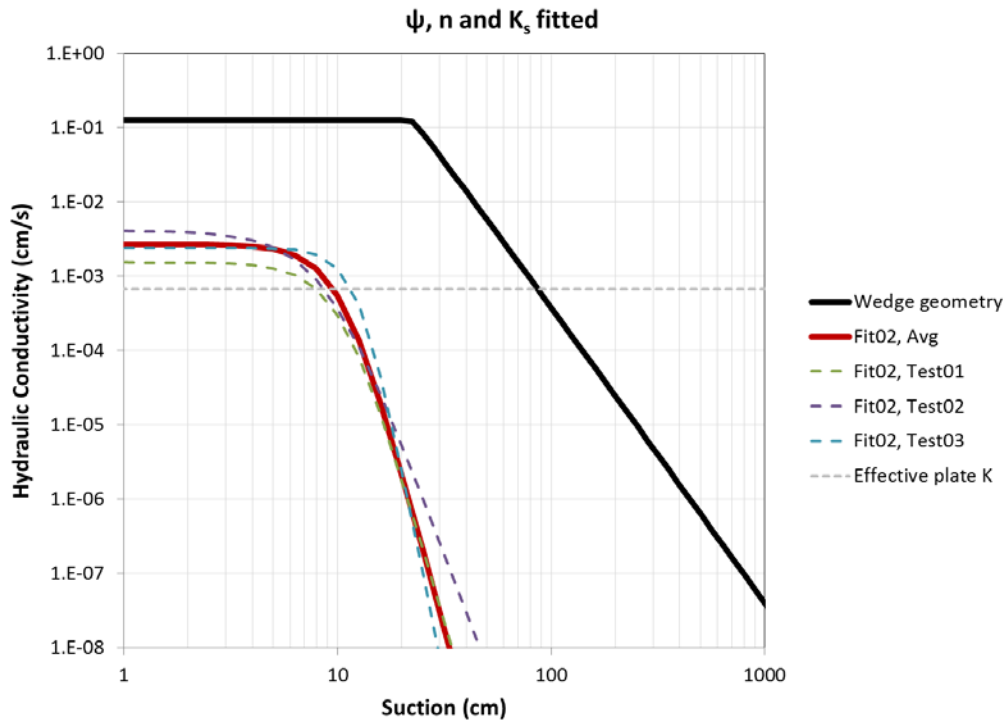
Figure 5-6. Inverse modeling fits compared to analytic wedge fracture solution – α, n and K_s fitted.

Figure 5-5 and Figure 5-6 also clearly indicate a lower air-entry pressure and steeper slope for the fitted curves than expected. The reason for these discrepancies is not clear. Most of the input parameters defining the analytic air-entry pressure (Equation (12)) are reasonably certain, a possible exception being the wetting angle. The adhesive tape used to shim one end of the slide pairs is significantly more hydrophobic than glass, which could lower the effective wetting angle. Other factors potentially influencing the wetting angle are components of the adhesive backing dissolving into the pore water, and a surface coating or film on the glass slides.

A series of informal desktop experiments were performed to assess the potential uncertainty in wetting angle that was assumed to be 25 degrees based on literature. A drop of water placed on the back (non-adhesive) side of a tape strip appeared to initially form a wetting angle of roughly 75 degrees; after several minutes the angle decreased to perhaps 45 to 50 degrees. Capillary rise was measured between glass plates separated by metal shims with total thicknesses ranging from 0.38 to 0.66 mm. Wetting angles from 42 to 56 degrees were required to reproduce the observed capillary rise using Equation (1). These observations support use of a larger wetting angle in the analytic solutions, perhaps has large as 50 degrees or so. However, a wetting angle of 75 degrees is required to reproduce the experimental data from outflow extraction method testing of the glass slide assemblage, as shown by Figure 5-7. An angle that large is not supported by the literature or informal observations from desktop experimentation.

Because of significant discrepancies between the measured and expected hydraulic conductivity curves, the outflow extraction method of Dixon and Nichols (2013) was not validated by this study. Neither was it invalidated considering considerable uncertainty in the appropriate wetting angle assumed in the reference analytic solution. Further development will be required to resolve these issues. Key recommendations for future work would be to

1) use hydrophilic shims when constructing the synthetic fracture test specimen,
2) avoid substances that may dissolve into the surrounding liquid and affect wetting angle or surface tension,
3) confirm the absence of surface coatings or contamination on glass plates,
4) measure the wetting angle for the selected liquid and solid materials,
5) confirm the air-entry pressure through static testing before proceeding to transient outflow testing.
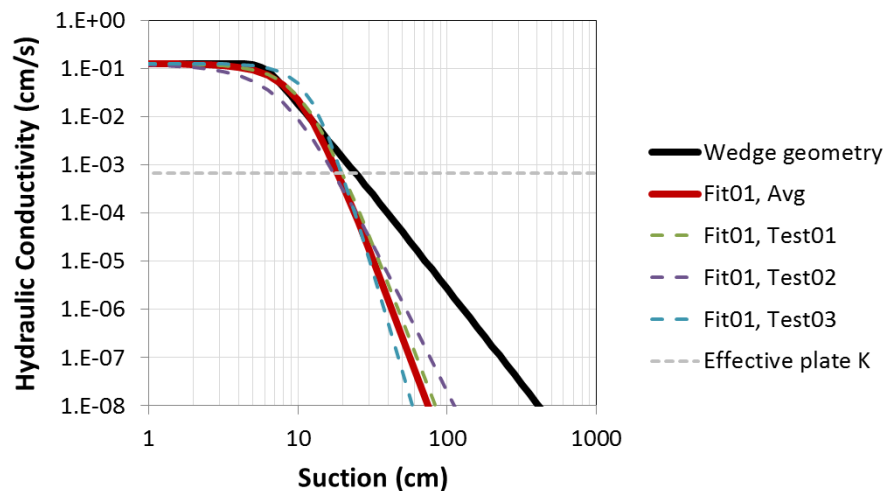
Figure 5-7. Analytic wedge solution for a wetting / contact angle empirically set to 75 degrees.

6.0 Fractured Cementitious Material Testing

Dixon and Nichols (2013) measured the unsaturated hydraulic conductivity of two fractured grout samples, identified as TR436 and TR437. Figure 6-1 and Figure 6-2 show the extent of cracking on these specimens through surface photography and interior radiography images. Micro-fracturing in both specimens was induced by oven drying. The TR436 sample also has a macro-fracture from being broken in half through mechanical loading. The TR437 sample was not broken, but nonetheless has one notably larger fracture among many smaller micro-cracks. No new outflow extraction method experimental data were acquired within the present study. However, further analysis of the existing data from Dixon and Nichols (2013) is presented herein. Figure 6-3 provides photographic images of the top and bottom of a third fractured grout specimen, TR430. This sample has a macro-fracture among smaller cracks. Outflow extraction method data from three tests were acquired within this study for TR430. Appendix B provides the experimental data used in inverse modeling for all five experiments. The saturated hydraulic conductivities of TR436 and TR437 were measured independent of outflow extraction testing with a flexible wall permeameter (ASTM D5084-03, Dixon and Nichols 2013). However, the saturated conductivity of TR430 has not been measured with this technique.

Table 6-1 through Table 6-5 summarize the inverse modeling matrices and results for the five experiments. Figure 6-4 through Figure 6-8 compare the measured and simulated cumulative flux leaving the bottom of the test specimen. Experimental data were processed from both the fracture-only and total area viewpoints where possible (e.g. TR436_1 versus TR436_1b). As with the synthetic fractured medium constructed from glass plates, practically the same vGM parameters result from the two approaches. The void volume is assumed to be completely emptied at the highest tested pressure, such that $\Theta_r = 0$. Total porosity or saturated liquid content Θ_s is assumed to correspond to the cumulative volume of extracted water for the total (fracture+matrix) area fitting cases. For TR436 and TR437 the fitted K_s value is roughly an order of magnitude lower than the independently measured value. Table 6-6 through Table 6-9 compare inverse modeling results obtained from the five tests for various combinations of fitted parameters. The estimated values of α and n are similar regardless of whether K_s is fitted (Table 6-6, Table 6-7). Fitting Θ_s, α and n produced unreasonably high values for saturated water content Θ_s or fracture volume (Table 6-8). Fitting all four parameters (Table 6-9) produced more parameter variability within and between cases, indicating lower uniqueness and higher uncertainty. The overall effect can be seen by comparing Figure 6-9 and Figure 6-10, which show unsaturated hydraulic conductivity from the three TR430 tests. In these figures the solid thickness line is the average curve, that is, the variation resulting from individually averaged vGM parameters.

Figure 6-11 through Figure 6-14 show the effective pressure plate conductivity defined in a preceding section. Here the effective plate conductivity is similar to the conductivity of the tested materials, and would not have significantly masked the K_s parameter in inverse fitting. Figure 6-11 through Figure 6-14 also compare unsaturated hydraulic conductivity for the three fractured grout specimens, and two soils commonly used in Savannah River PAs and SAs to represent degraded cementitious materials. Discounting Figure 6-13, representing inverse fitting results with excessively large Θ_s, and Figure 6-14, representing less reliable parameter estimates, nominal hydraulic conductivity for the fractured cementitious materials decreases with a steeper slope than nominal K_s for soils (Figure 6-11, Figure 6-12). Assuming that lower hydraulic conductivity is conservative with respect to facility performance, these figures suggest that soils may serve as reasonable surrogates for damaged cementitious materials, provided their saturated conductivity is sufficiently large.

(a)

(b)

(c)

(d)
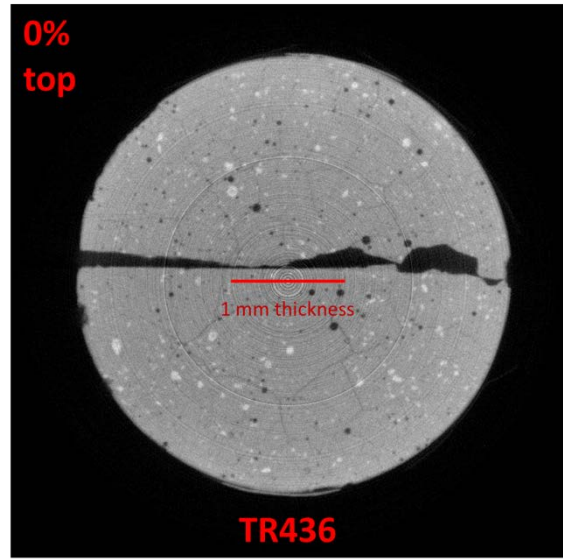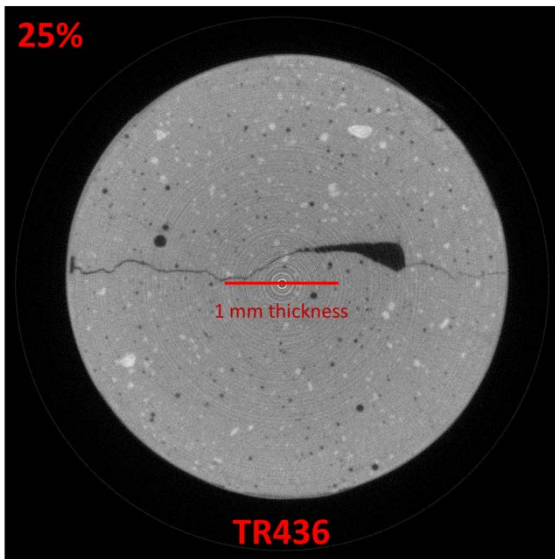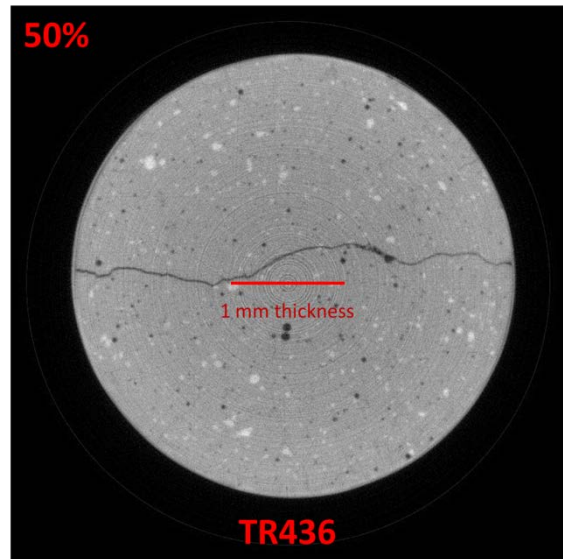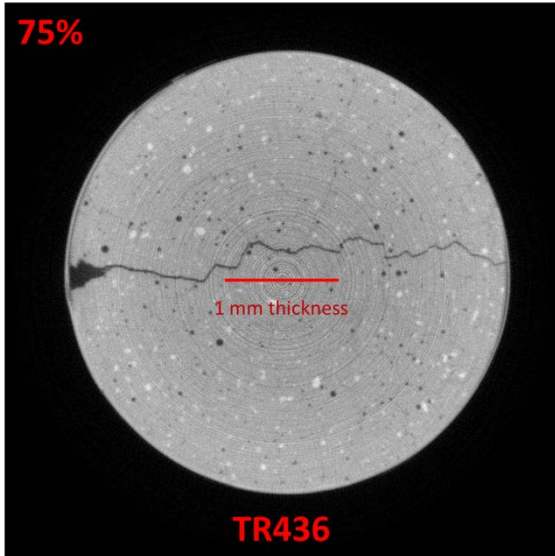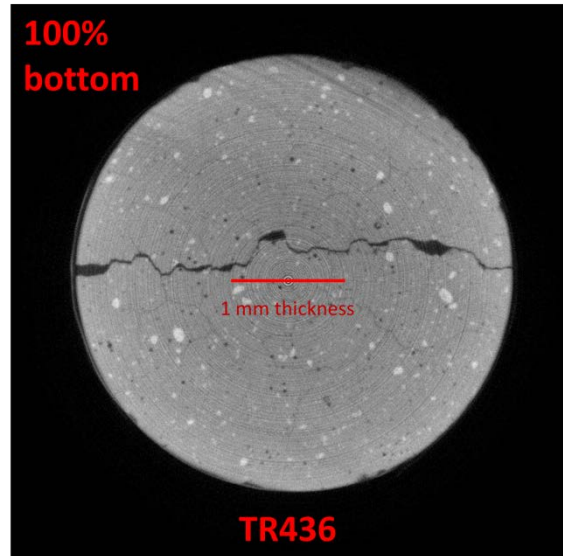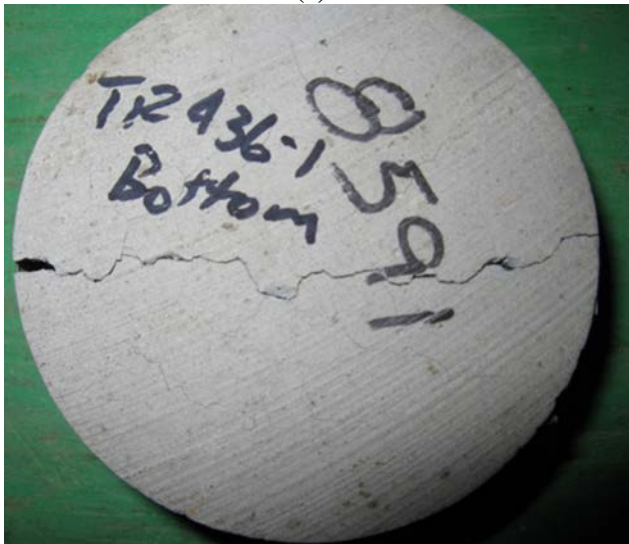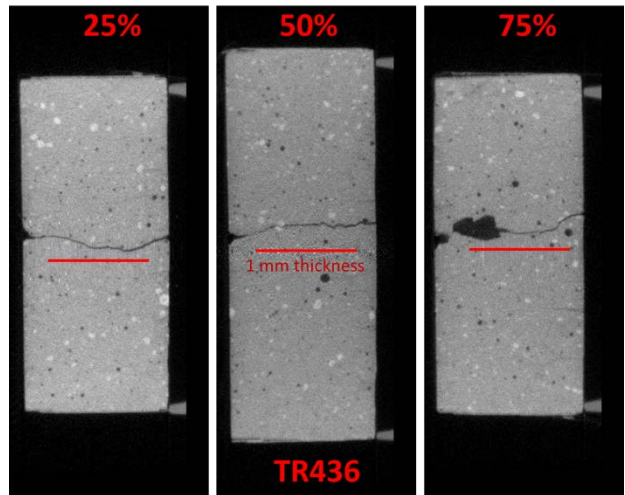
Figure 6-1. Photography and radiography images for fractured grout specimen TR436.

(a)

(b)

(c)

(d)

(e)

(f)

(g)
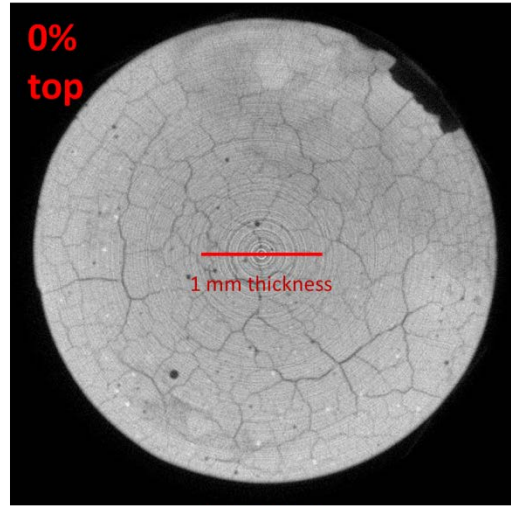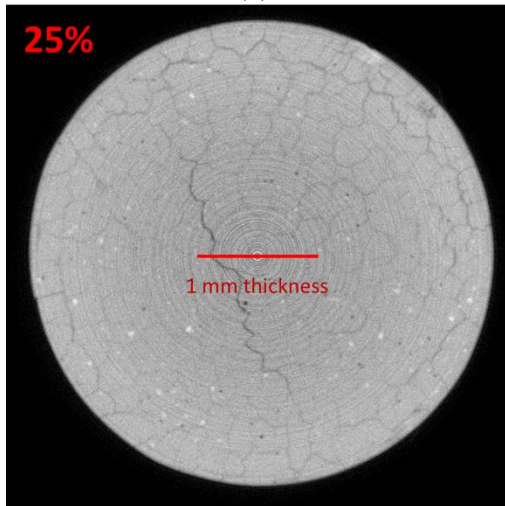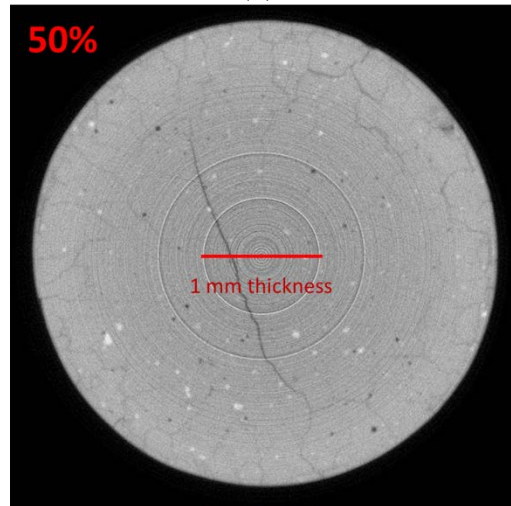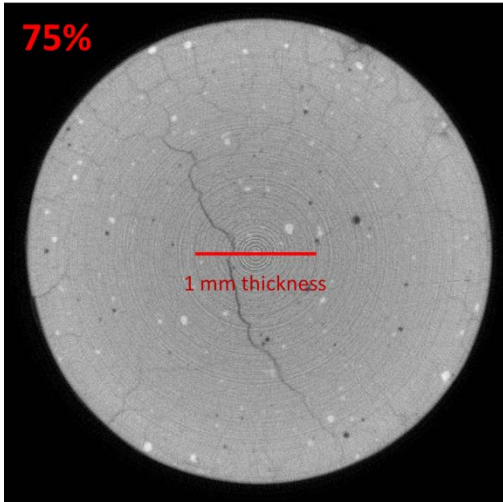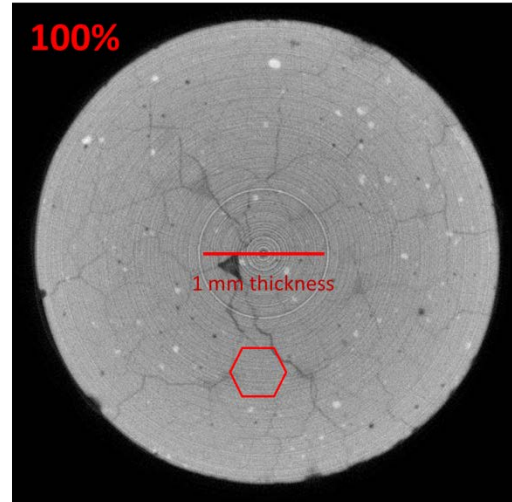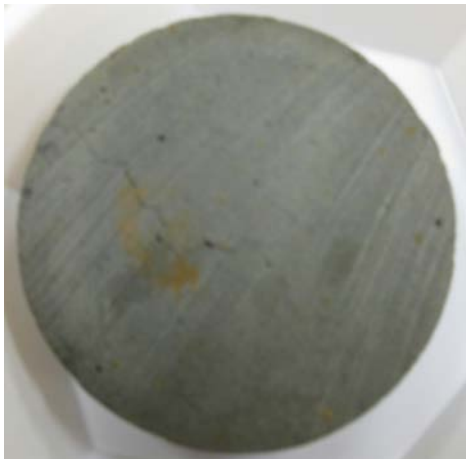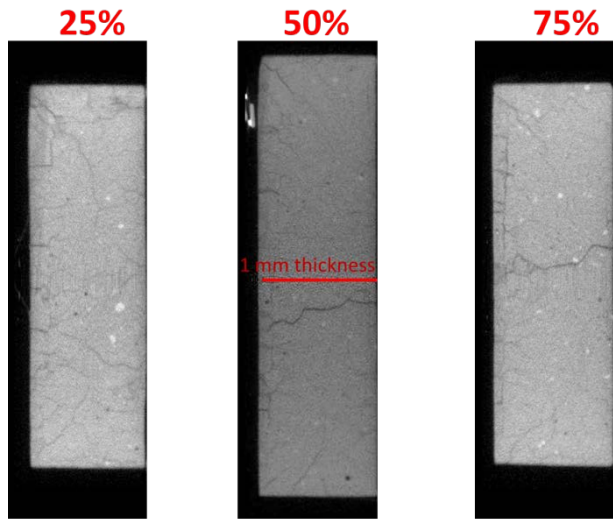
(h)

Figure 6-2. Photography and radiography images for fractured grout specimen TR437.

(a) Top   **(b) Bottom**

Figure 6-3. Photography images for fractured grout specimen TR430.

Table 6-1. Inverse modeling matrix and results – TR436 specimen.

(a) Inverse modeling matrix

Case	θ_r	θ_s	α	n	K_s fracture (cm/s)	K_s total (cm/s)	Comment
TR436_1	0	1	fitted	fitted	fitted	fitted	Fracture
TR436_2	0	1	fitted	fitted	1.36E-03	1.99E-05	Fracture
TR436_1b	0	0.0146	fitted	fitted	fitted	fitted	Fracture + Matrix
TR436_2b	0	0.0146	fitted	fitted	1.36E-03	1.99E-05	Fracture + Matrix
TR436_3b	0	fitted	fitted	fitted	1.36E-03	1.99E-05	Fracture + Matrix
TR436_4b	0	fitted	fitted	fitted	fitted	fitted	Fracture + Matrix

(b) Inverse modeling results

Case	θ_r	θ_s	α	n	K_s fracture (cm/s)	K_s total (cm/s)	R^2
TR436_1	0	1	0.0122	2.34	1.75E-04	2.56E-06	0.945
TR436_2	0	1	0.0121	2.15	1.36E-03	1.99E-05	0.927
TR436_1b	0	0.0146	0.0123	2.31	1.96E-04	2.87E-06	0.944
TR436_2b	0	0.0146	0.0125	2.12	1.36E-03	1.99E-05	0.925
TR436_3b	0	0.0745	0.0125	1.12	1.36E-03	1.99E-05	0.976
TR436_4b	0	0.0384	0.0133	1.25	5.09E-04	7.44E-06	0.977

Table 6-2. Inverse modeling matrix and results – TR437 specimen.

(a) Inverse modeling matrix

Case	θ_r	θ_s	α	n	K_s fracture (cm/s)	K_s total (cm/s)	Comment
TR437_1	0	1	fitted	fitted	fitted	fitted	Fracture
TR437_2	0	1	fitted	fitted	8.37E-03	1.42E-04	Fracture
TR437_1b	0	0.0170	fitted	fitted	fitted	fitted	Fracture + Matrix
TR437_2b	0	0.0170	fitted	fitted	8.37E-03	1.42E-04	Fracture + Matrix
TR437_3b	0	fitted	fitted	fitted	8.37E-03	1.42E-04	Fracture + Matrix
TR437_4b	0	fitted	fitted	fitted	fitted	fitted	Fracture + Matrix

(b) Inverse modeling results

Case	θ_r	θ_s	α	n	K_s fracture (cm/s)	K_s total (cm/s)	R^2
TR437_1	0	1	0.0221	2.22	4.73E-04	8.02E-06	0.981
TR437_2	0	1	0.0212	1.91	8.37E-03	1.42E-04	0.920
TR437_1b	0	0.0170	0.0219	2.22	4.84E-04	8.21E-06	0.981
TR437_2b	0	0.0170	0.0214	1.90	8.37E-03	1.42E-04	0.920
TR437_3b	0	0.0539	0.0396	1.13	8.37E-03	1.42E-04	0.955
TR437_4b	0	0.0158	0.0216	2.61	4.11E-04	6.97E-06	0.982

Table 6-3. Inverse modeling matrix and results – TR430 specimen, Test1.

(a) Inverse modeling matrix

Case	θ_r	θ_s	α	n	K_s fracture (cm/s)	K_s total (cm/s)	Comment
TR430.1_1	0	1	fitted	fitted	fitted	fitted	Fracture
TR430.1_1b	0	0.0109	fitted	fitted	fitted	fitted	Fracture + Matrix
TR430.1_4b	0	fitted	fitted	fitted	fitted	fitted	Fracture + Matrix

(b) Inverse modeling results

Case	θ_r	θ_s	α	n	K_s fracture (cm/s)	K_s total (cm/s)	R^2
TR430.1_1	0	1	0.0138	2.14	1.49E-04	1.62E-06	0.973
TR430.1_1b	0	0.0109	0.0134	2.14	2.11E-04	2.29E-06	0.971
TR430.1_4b	0	0.0099	0.0121	3.28	6.93E-05	7.54E-07	0.981

Table 6-4. Inverse modeling matrix and results – TR430 specimen, Test2.

(a) Inverse modeling matrix

Case	θ_r	θ_s	α	n	K_s fracture (cm/s)	K_s total (cm/s)	Comment
TR430.2_1	0	1	fitted	fitted	fitted	fitted	Fracture
TR430.2_1b	0	0.0135	fitted	fitted	fitted	fitted	Fracture + Matrix
TR430.2_4b	0	fitted	fitted	fitted	fitted	fitted	Fracture + Matrix

(b) Inverse modeling results

Case	θ_r	θ_s	α	n	K_s fracture (cm/s)	K_s total (cm/s)	R^2
TR430.2_1	0	1	0.0398	1.75	2.14E-03	2.89E-05	0.950
TR430.2_1b	0	0.0135	0.0430	1.71	3.36E-03	4.54E-05	0.950
TR430.2_4b	0	0.0221	0.0566	1.26	1.25E-02	1.69E-04	0.974

Table 6-5. Inverse modeling matrix and results – TR430 specimen, Test3.

(a) Inverse modeling matrix

Case	θ_r	θ_s	α	n	K_s fracture (cm/s)	K_s total (cm/s)	Comment
TR430.3_1	0	1	fitted	fitted	fitted	fitted	Fracture
TR430.3_1b	0	0.0086	fitted	fitted	fitted	fitted	Fracture + Matrix
TR430.3_4b	0	fitted	fitted	fitted	fitted	fitted	Fracture + Matrix

(b) Inverse modeling results

Case	θ_r	θ_s	α	n	K_s fracture (cm/s)	K_s total (cm/s)	R^2
TR430.3_1	0	1	0.0127	2.86	1.32E-03	1.14E-05	0.971
TR430.3_1b	0	0.00859	0.0125	2.86	1.60E-03	1.38E-05	0.971
TR430.3_4b	0	0.00886	0.0135	2.54	1.27E-03	1.09E-05	0.974

Table 6-6. Summary of inverse modeling results for fitted α and n.

Case, Test	θ_r	θ_s	α (cm^{-1})	n	K_s total area (cm/s)
TR436	0	0.0146	0.012	2.1	2.0E-05
TR437	0	0.0170	0.021	1.9	1.4E-04

Table 6-7. Summary of inverse modeling results for fitted α, n and K_s.

Case, Test	θ_r	θ_s	α (cm^{-1})	n	K_s total area (cm/s)
TR436	0	0.0146	0.012	2.3	2.7E-06
TR437	0	0.0170	0.022	2.2	8.1E-06
TR430	0	0.0110	0.023	2.2	1.6E-05
TR430 test1	0	0.0109	0.014	2.1	2.0E-06
TR430 test2	0	0.0135	0.041	1.7	3.7E-05
TR430 test3	0	0.0086	0.013	2.9	1.3E-05

Table 6-8. Summary of inverse modeling results for fitted Θ_s, α and n.

Case, Test	θ_r	θ_s	α (cm^{-1})	n	K_s total area (cm/s)
TR436	0	0.0745	0.012	1.1	2.0E-05
TR437	0	0.0539	0.040	1.1	1.4E-04

Table 6-9. Summary of inverse modeling results for fitted Θ_s, α, n and K_s.

Case, Test	θ_r	θ_s	α (cm^{-1})	n	K_s total area (cm/s)
TR436	0	0.0384	0.013	1.2	7.4E-06
TR437	0	0.0158	0.022	2.6	7.0E-06
TR430	0	0.0136	0.027	2.4	6.0E-05
TR430 test1	0	0.0099	0.012	3.3	7.5E-07
TR430 test2	0	0.0221	0.057	1.3	1.7E-04
TR430 test3	0	0.0089	0.013	2.5	1.1E-05

(a) α, n fitted

(b) α, n, K$_s$ fitted

(c) θ, α, n fitted
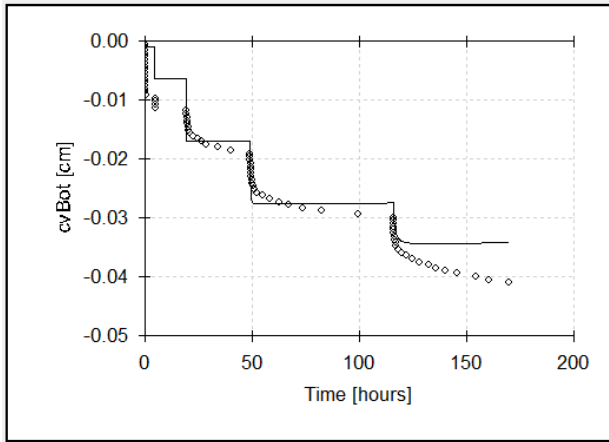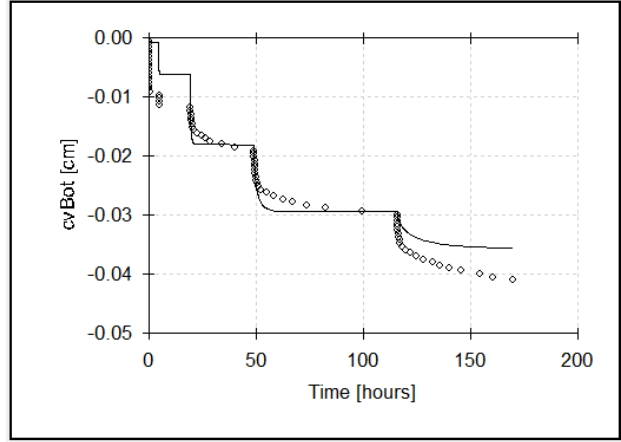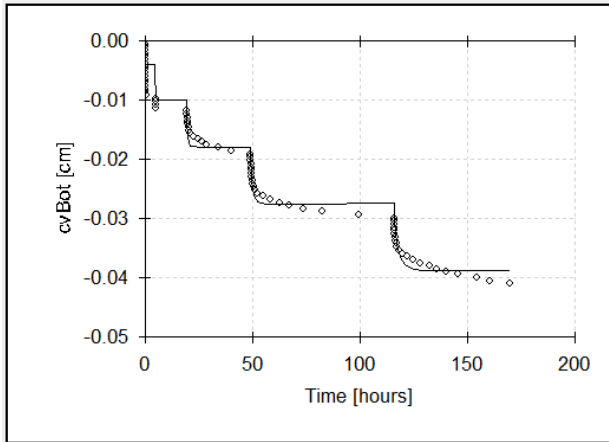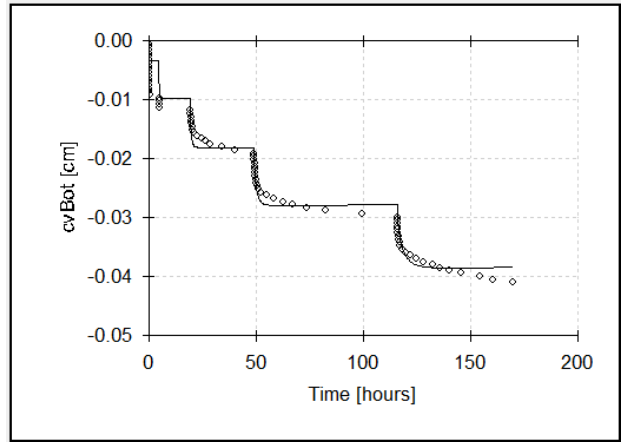
(d) θ, α, n, K$_s$ fitted

○ = measured data   — = model simulation

Figure 6-4. Measured and simulated cumulative flux for TR436.

(a) α, n fitted

(b) α, n, K$_s$ fitted

(c) θ, α, n fitted
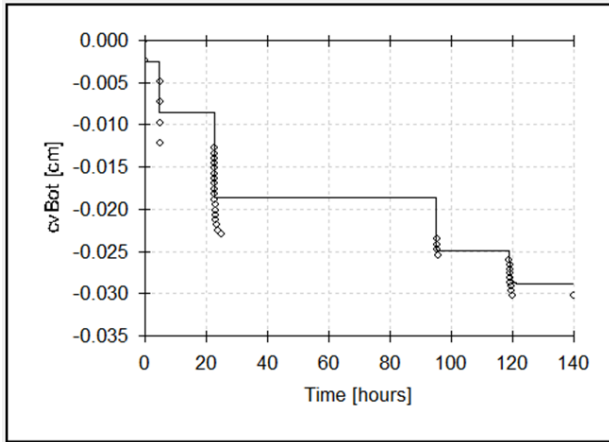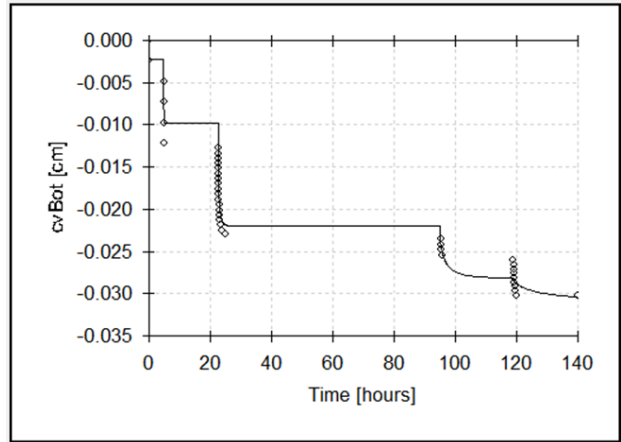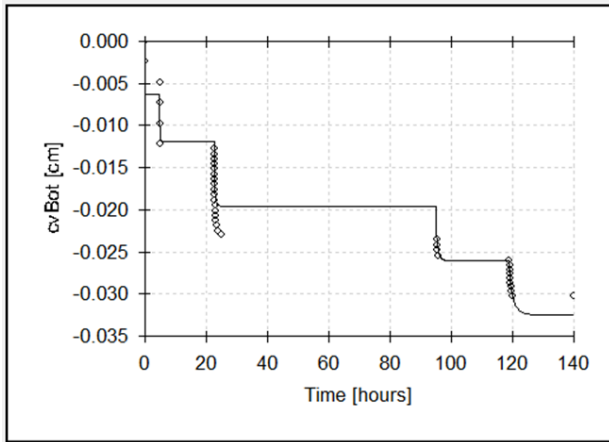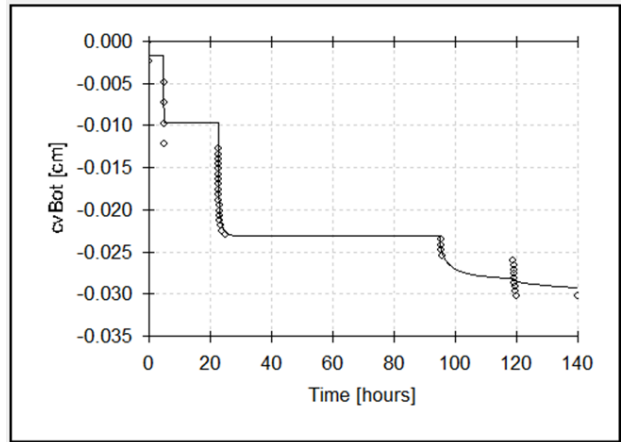
(d) θ, α, n, K$_s$ fitted

○ = measured data   — = model simulation

Figure 6-5. Measured and simulated cumulative flux for TR437.

(a) α, n fitted

(b) α, n, K$_s$ fitted

(c) θ, α, n fitted

(d) θ, α, n, K$_s$ fitted

○ = measured data   — = model simulation

Figure 6-6. Measured and simulated cumulative flux for TR430, Test 1.
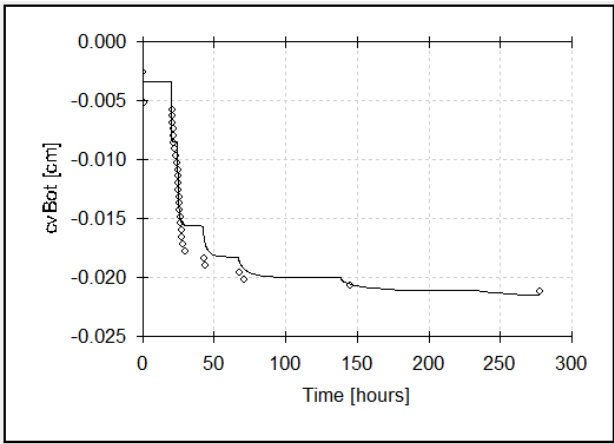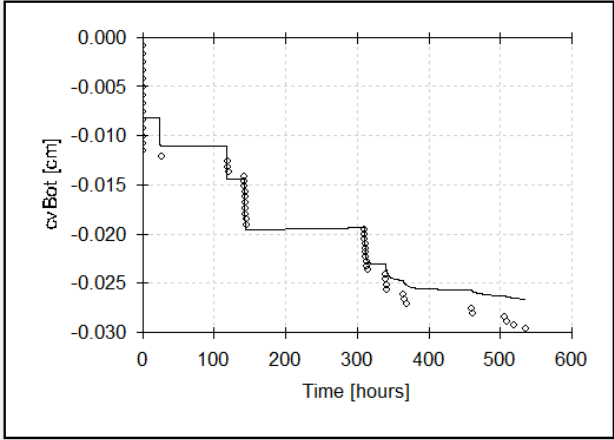
Not applicable: K_s not independently measured	
(a) α, n fitted	(b) α, n, K_s fitted
Not applicable: K_s not independently measured	
(c) θ, α, n fitted	(d) θ, α, n, K_s fitted
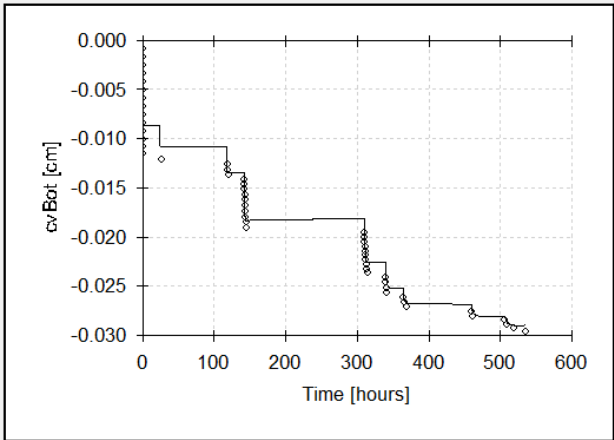
○ = measured data   —— = model simulation

Figure 6-7. Measured and simulated cumulative flux for TR430, Test 2.

(a) α, n fitted

(b) α, n, K$_s$ fitted

(c) θ, α, n fitted
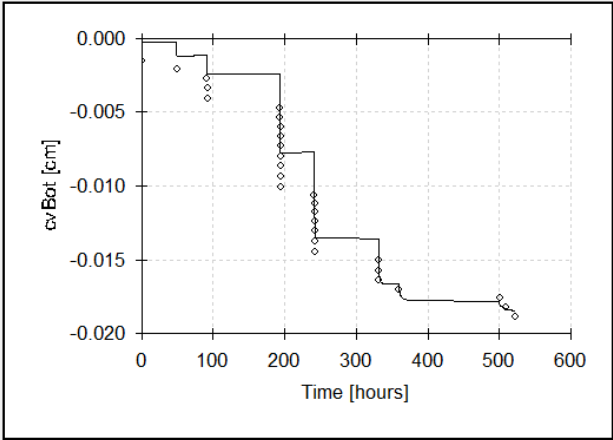
(d) θ, α, n, K$_s$ fitted

○ = measured data   — = model simulation

Figure 6-8. Measured and simulated cumulative flux for TR430, Test 3.
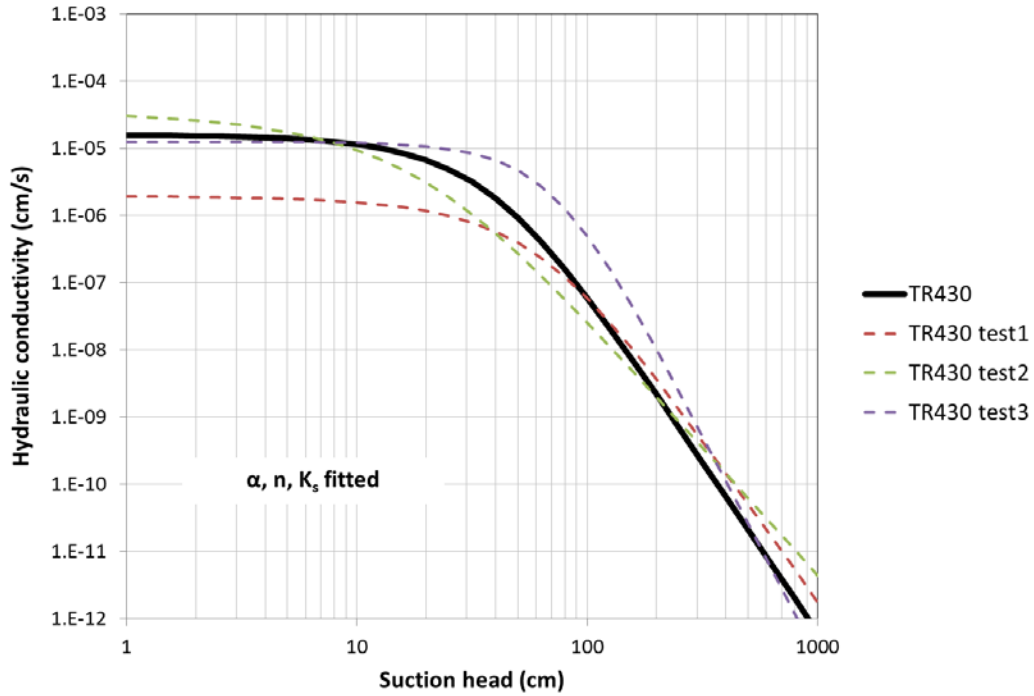
Figure 6-9. Unsaturated hydraulic conductivity from TR430 tests for fitted α, n and K_s.
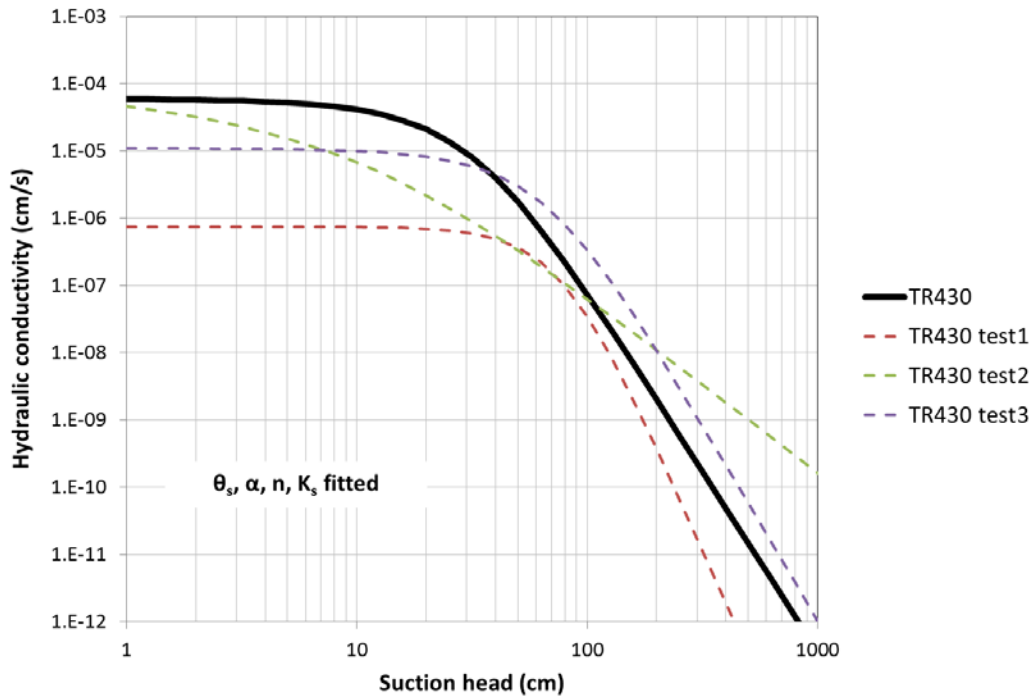
Figure 6-10. Unsaturated hydraulic conductivity from TR430 tests for fitted Θ_s, α, n and K_s.
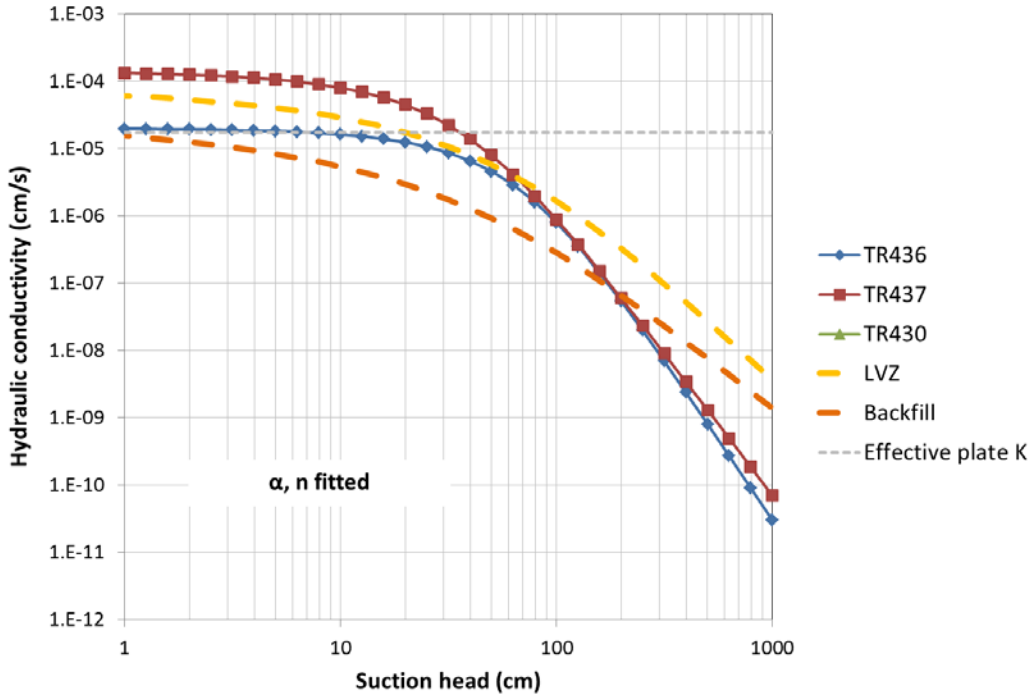
Figure 6-11. Unsaturated hydraulic conductivity for fitted α and n.
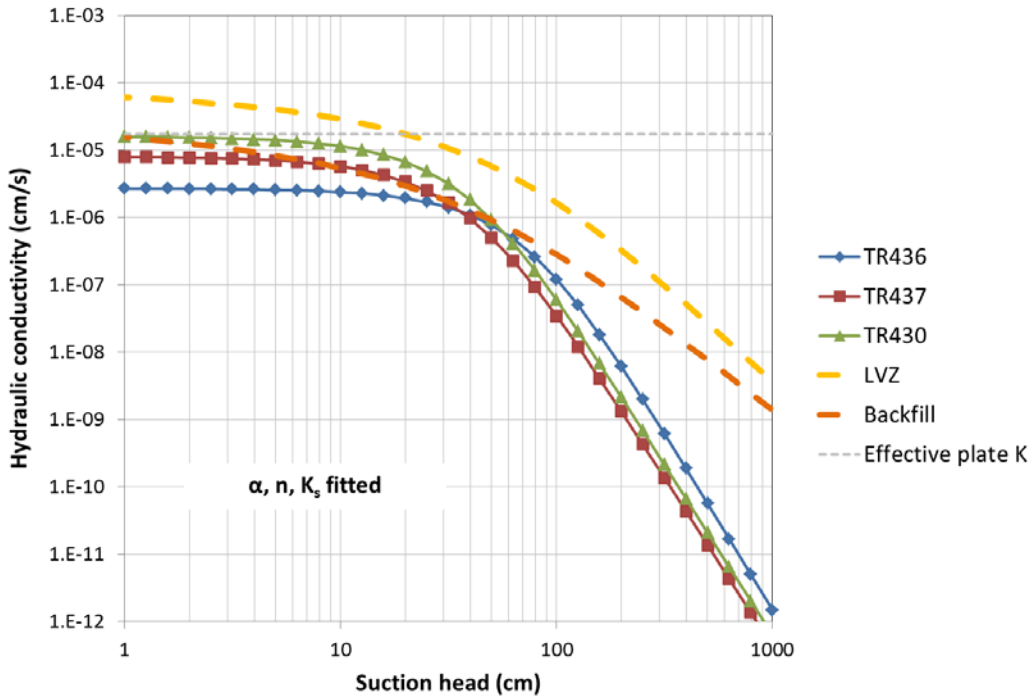
Figure 6-12. Unsaturated hydraulic conductivity for fitted α, n and K_s.

46
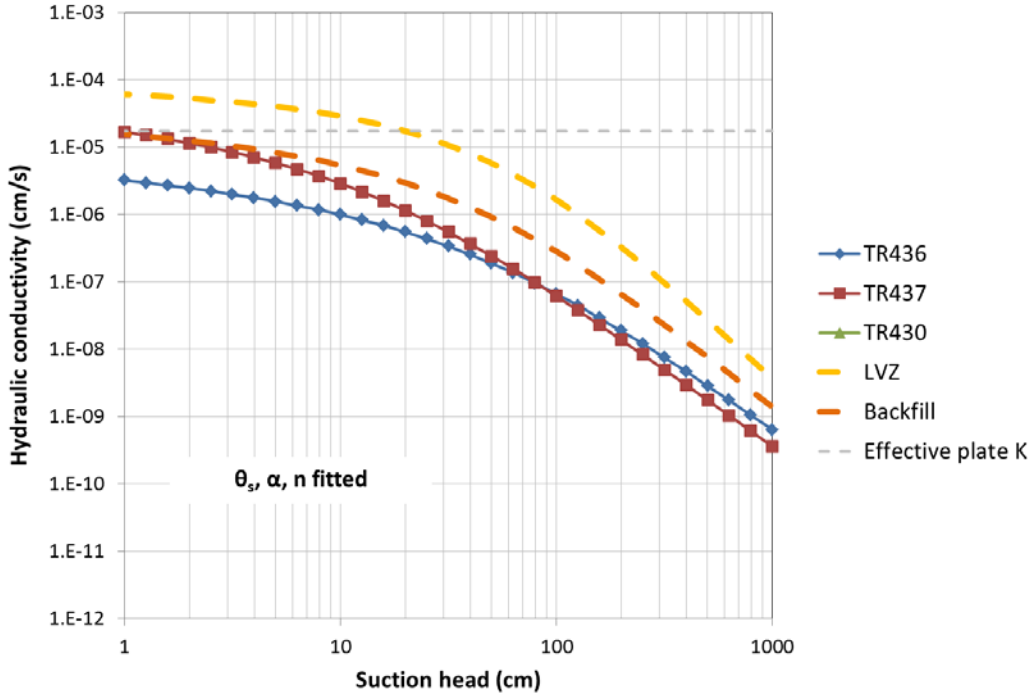
Figure 6-13. Unsaturated hydraulic conductivity for fitted Θ_s, α and n.
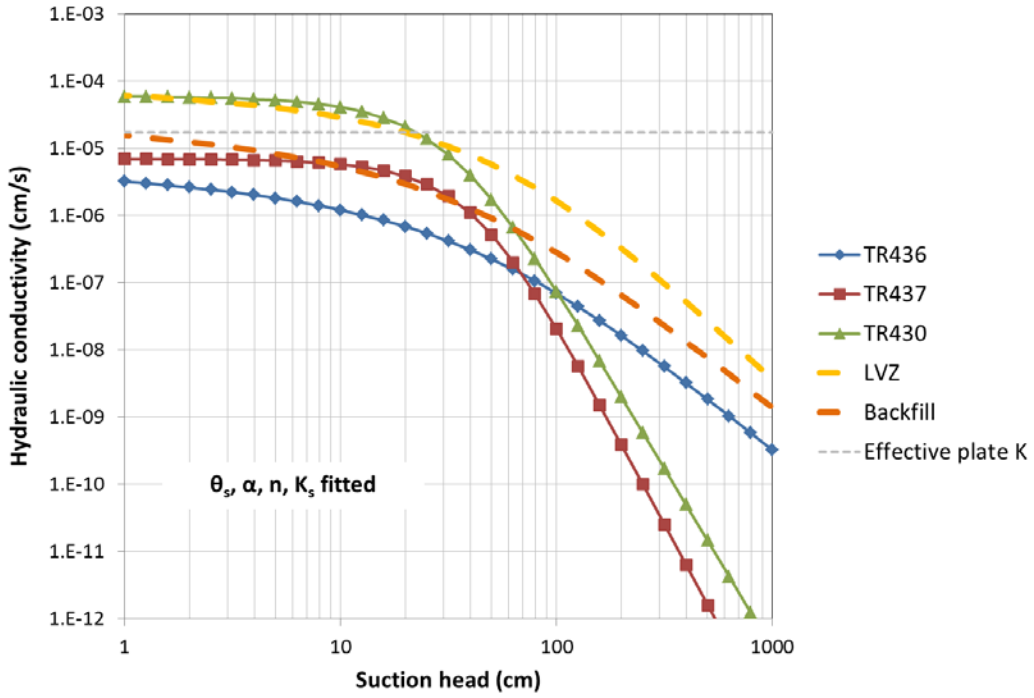
Figure 6-14. Unsaturated hydraulic conductivity for fitted Θ_s, α, n and K_s.

7.0 Conclusions

Dixon and Nichols (2013) developed an experimental method for measuring the unsaturated hydraulic conductivity of fractured materials by modifying a standard test apparatus and procedure suitable for testing granular soils. To validate the technique using a reference material with known unsaturated properties, a synthetic fractured medium composed of a series of glass plates shimmed at one end was conceived and constructed. Shimming at one end produced a wedge-shaped aperture, a geometry amenable to analysis. Analytic solutions for saturation and relative permeability were derived for the wedge geometry. A test specimen was constructed from 51 glass microscope slides by shimming one end with a thin strip of adhesive tape. van Genuchten (1980) / Mualem (1976) parameters defining water retention and relative permeability curves were estimated for three outflow extraction experiments. The fitted parameters from the three tests are consistent, but do not produce characteristic curves in agreement with the analytic solution. The reason for the discrepancy is unknown. A potential explanation is uncertainty in the wetting angle assumed for water on glass, due to the presence of hydrophobic tape shims, dissolved adhesive, a coating or contamination on the microscope slides used as glass plates, or other factor. Because of the observed discrepancies between the expected and observed behavior of the reference specimen, the technique of Dixon and Nichols (2013) could not be validated. However, neither was the method invalidated considering considerable uncertainty in the appropriate wetting angle to use in the analytic solution.

Notwithstanding difficulties with validating the test method, an additional fractured grout sample TR430 was tested three times with the method Dixon and Nichols (2013). Characteristic curve parameters were estimated through inverse modeling using HYDRUS-1D. Data from the three TR430 tests are similar indicating some level of reproducibility in estimated parameters, despite variable pressure steps and durations. Existing data from samples TR436 and TR437 collected previously by Dixon and Nichols (2013) were further analyzed. Compared to soils, hydraulic conductivity as a function of suction/tension head for the fractured cementitious materials was observed to have a steeper negative slope. Assuming that lower hydraulic conductivity is conservative with respect to facility performance, these comparisons suggest that soils may serve as reasonable surrogates for damaged cementitious materials, provided their saturated conductivities are sufficiently large.

8.0 References

Altman, S. J., B. W. Arnold, R. W. Barnard, G. E. Barr, C. K. Ho, S. A. McKenna, and R. R. Eaton. *Flow Calculations for Yucca Mountain Groundwater Travel Time (GWTT-95)*. Sandia Report SAND96-0819. September 1996.

Barraza, H. J., S. Kunapuli, and E. A. O'Rear. *Advancing Contact Angles of Newtonian Fluids During "High" Velocity, Transient, Capillary-Driven Flow in a Parallel Plate Geometry*. J. Phys. Chem. B 106, 4979-4987. 2002.

Cementitious Barriers Partnership. *Review of Mechanistic Understanding and Modeling and Uncertainty Analysis Methods For Predicting Cementitious Barrier Performance*. CBP-TR-2009-002, Rev.0. November 2009.

Chen, C. *Liquid-Gas Relative Permeabilities in Fractures: Effects of Flow Structures, Phase Transformation and Surface Roughness*. Stanford University. 2005.

Chen, C.-Y. and R. N. Horne. *Two-Phase Flow in Rough-Walled Fractures: Experiments and a Flow Structure Model*. Water Resources Research vol. 42. W03430, doi:10.1029/2004WR003837. 2006.

Dixon, K. L. and R. L. Nichols. *Method Development for Determining the Hydraulic Conductivity of Fractured Porous Media*. SRNL-STI-2013-00522, Rev. 0. September 2013.

Eching, S. O. and J. W. Hopmans. *Optimization of Hydraulic Functions from Transient Outflow and Soil Water Pressure Data*. Soil Science Society of America Journal vol. 57 no. 5 p. 1167-1175. 1993.

Finn, R. *Capillary Surface Interfaces*. Notices of the AMS, volume 46, number 7. 770-781 http://www.ams.org/notices/199907/fea-finn.pdf. August 1999.

Firoozabadi, A. and J. Hauge. *Capillary pressure in fractured porous media*. J. Pet. Technol. p. 784–791. June 1990.

Flach, G. P. and F. G. Smith III. *Degradation Of Cementitious Materials Associated with Saltstone Disposal Units*. SRNL-STI-2013-00118, Rev. 2. September 2014.

Flach, G. P. and G. A. Taylor. *PORFLOW Modeling Supporting the FY14 Saltstone Special Analysis*. SRNL-STI-2014-00083, Rev. 1. April 2014a.

Flach, G. P. and G. A. Taylor. *Sensitivity Analysis for Saltstone Disposal Unit Column Degradation Analyses*. SRNL-STI-2014-00505, Rev. 0. October 2014b.

Hauksbee, F. *An Account of an Experiment Touching the Ascent of Water between Two Glass Planes, in a Hyperbolick Figure*. Philosophical Transactions (1683-1775) vol. 27 (1710-1712) p. 539-540. 1712.

Higuera, F. J., A. Medina, and A. Liñán. *Capillary rise of a liquid between two vertical plates making a small angle*. PHYSICS OF FLUIDS 20, 102102. 2008.

Hopmans, J. W., J. Šimůnek, N. Romano and W. Durner. *Inverse Modeling of Transient Water Flow, In: Methods of Soil Analysis, Part 1, Physical Methods, Chapter 3.6.2*. Eds. J. H. Dane and G. C. Topp. Third edition. SSSA. Madison, WI. p. 963-1008. 2002.

Jordan, J. M. and G. P. Flach. *PORFLOW Modeling Supporting the FY13 Saltstone Special Analysis*. SRNL-STI-2013-00280, Rev. 0. May 2013.

Jordan, J. M., G. P. Flach and M. L. Westbrook. *PORFLOW Modeling Supporting the H-Tank Farm Performance Assessment*. SRNL-STI-2012-00465, Rev. 0. August 2012.

Kool, J. B. and J. C. Parker. *Analysis of the Inverse Problem for Transient Unsaturated Flow*. Water Resources Research vol. 24 no. 6 p. 817-830. 1988.

Langton, C. A. *Chemical Degradation Assessment for the H-Area Tank Farm Concrete Tanks and Fill Grouts*. SRNL-STI-2010-00035, Rev. 0. January 2010.

Li, D., Editor. *Encyclopedia of Microfluidics and Nanofluidics, Volume 1*. Springer Science & Business Media. 2008.

Li, Y., Y.-F. Chen and C.-B. Zhou. *Hydraulic Properties of Partially Saturated Rock Fractures Subjected to Mechanical Loading*. Engineering Geology vol. 179. p. 24-31. 2014.

Liu, H.-H. and G. S. Bodvarsson. *Constitutive Relations for Unsaturated Flow in a Fracture Network*. Journal of Hydrology vol. 252. p. 116-125. 2001.

Monachesi, L. B. and L. Guarracino. *A Fractal Model for Predicting Water and Air Permeabilities of Unsaturated Fractured Rocks*. Transport in Porous Media vol. 90. p. 779-789. doi 10.1007/s11242-011-9815-9. 2011.

Mualem, Y. *A new model for predicting the hydraulic conductivity of unsaturated porous media*. Water Resour. Res. vol. 12 no. 3 p. 513–522. doi:10.1029/WR012i003p00513. 1976.

Or, D. and M. Tuller. *Flow in unsaturated fractured porous media: Hydraulic conductivity of rough surfaces*. Water Resources Research vol. 36 no. 5. p. 1165-1177, May 2000.

Persoff, P. and K. Pruess. *Two-phase flow visualization and relative permeability measurement in natural rough-walled rock fractures*. Water Resour. Res. vol. 31 no. 5. p. 1175–1186. 1995.

Prakash, S. and J. Yeom. *Nanofluidics and Microfluidics: Systems and Applications*. William Andrew. 312 pages. 2014.

Pruess, K. *On water seepage and fast preferential flow in heterogeneous, unsaturated rock fractures*. Journal of Contaminant Hydrology vol. 30. p. 333–362. 1998.

Pruess, K. and Y. W. Tsang. *On Two-Phase Relative Permeability and Capillary Pressure of Rough-Walled Rock Fractures*. Water Resources Research vol. 26 no. 9. p. 1915-1926. 1990.

Savannah River Remediation LLC. *FY2013 Special Analysis for the Saltstone Disposal Facility at the Savannah River Site*. SRR-CWDA-2013-00062, Rev. 1. June 2013.

Savannah River Remediation LLC. *FY2014 Special Analysis for the Saltstone Disposal Facility at the Savannah River Site*. SRR-CWDA-2014-00006, Rev. 1. June 2014.

Savannah River Remediation LLC. *Performance Assessment for the H-Area Tank Farm at the Savannah River Site*. SRR-CWDA-2010-00128, Rev. 1. November 2012.

Schwiebert, M.K. and W.H. Leong. *Underfill flow as viscous flow between parallel plates driven by capillary action*, Components, Packaging, and Manufacturing Technology, Part C, IEEE Transactions on , vol.19, no.2, pp.133,137. doi: 10.1109/3476.507149. Apr 1996.

Siebold, A., M. Nardin, J. Schultz, A. Walliser, and M. Oppliger. *Effect of dynamic contact angle on capillary rise phenomena*. Colloids and Surfaces A: Physicochemical and Engineering Aspects 161. 81–87. 2000.

Šimůnek, J., M. Th. van Genuchten, and M. Sejna. *The Hydrus-1D Software Package for Simulating the One-Dimensional Movement of Water, Heat, and Multiple Solutes in Variably-Saturated Media, Version 4.14*. Department of Environmental Sciences, University of California-Riverside, Riverside, CA, 92521. 2008.

SRR Closure & Waste Disposal Authority. *Performance Assessment for the Saltstone Disposal Facility at the Savannah River Site*. SRR-CWDA-2009-00017, Rev. 0. October 2009.

Streeter, V. L. and E. B. Wylie. *Fluid Mechanics, Seventh Edition*. McGraw-Hill. 1979.

Sumner, A. L., E. J. Menke, Y. Dubowski, J. T. Newberg, R. M. Penner, J. C. Hemminger, L. M. Wingen, T. Brauers, B. J. Finlayson–Pitts. *The nature of water on surfaces of laboratory systems and implications for heterogeneous chemistry in the troposphere*. Phys. Chem. Chem. Phys. vol. 6, p. 604-613. 2004.

Sung, J., Y.B. Kim, M.H. Lee. *Transient Phenomena of Dynamic Contact Angle in Micro Capillary Flow*. 15th International Symposium on Flow Visualization, Minsk, Belarus. June 25-28, 2012.

Taylor, B. *Part of a Letter from Mr. Brook Taylor, F. R. S. to Dr. Hans Sloane R. S. Secr. Concerning the Ascent of Water between Two Glass Plates*. Philosophical Transactions (1683-1775) vol. 27 (1710-1712) p. 538. 1712.

Tuller, M. and D. Or. *Unsaturated Hydraulic Conductivity of Structured Porous Media: A Review of Liquid Configuration–Based Models*. Vadose Zone Journal vol. 1. p. 14–37. August 2002.

van Genuchten, M. T. *A closed-form equation for predicting the hydraulic conductivity of unsaturated soils*. Soil Science Society America Journal vol. 44 no. 5 pp. 892-898. 1980.

Vargaftik, N. B., B. N. Volkov and L. D. Voljak. *International Tables of the Surface Tension of Water*. J. Phys. Chem. Ref. Data vol. 12 no. 3. 1983.

Wang, J. S. Y. and T. N. Narasimhan. *Hydrologic Mechanisms Governing Fluid Flow in a Partially Saturated, Fractured, Porous Medium*. Water Resour. Res. vol. 21 no. 12 p. 1861–1874. doi:10.1029/WR021i012p01861, 1985.

This intentional left blank

Appendix A. Data from Method Validation Experiments

Test01 Data:

Data summary
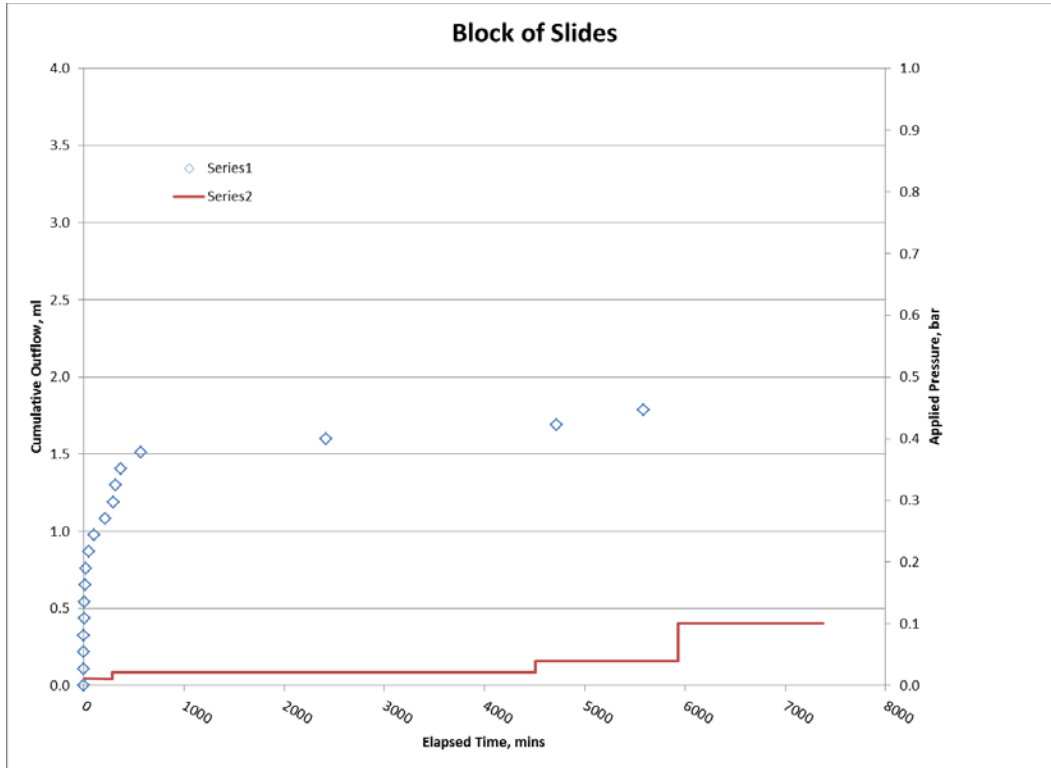
Pressure steps

Elapsed Time (hr)	Pressure (cm H2O)
0	11.52311046
4.782222222	11.21718718
4.7825	21.92450221
75.14944444	21.92450221
75.14972222	40.78977156
98.91694444	40.78977156
98.91722222	103.5040453
122.9172222	103.5040453

Cumulative flux based on total area

Time (h)	Cumulative flux (cm)
0.000	0.00E+00
0.003	-0.0042411
0.022	-0.0084705
0.044	-0.012696
0.074	-0.0169176
0.118	-0.0211353
0.203	-0.0253453
0.410	-0.0295474
0.872	-0.0338158
1.721	-0.0380491
3.595	-0.0421811
4.920	-0.0463599
5.292	-0.050562
6.174	-0.0547564
9.559	-0.0587911
40.364	-0.0622844
78.636	-0.0658829
93.166	-0.0696567
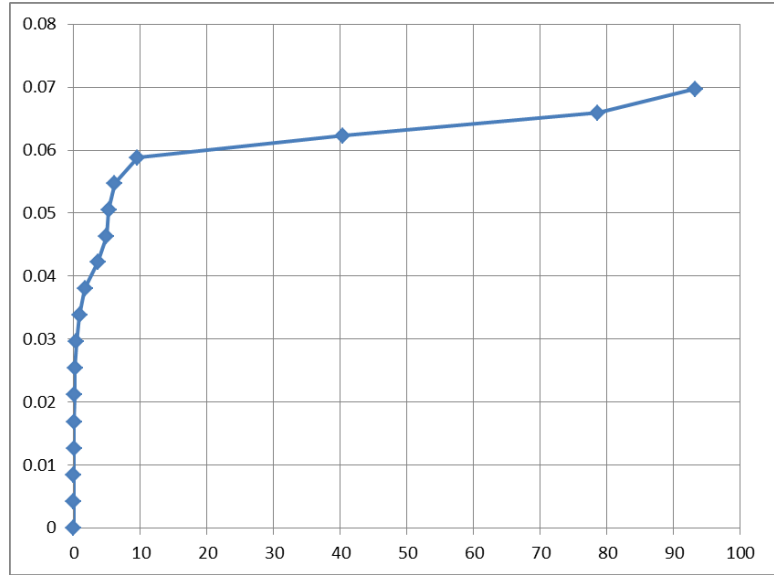
Cumulative flux based on fracture area

Time (h)	Cumulative flux (cm)
0.000	0.00E+00
0.003	-0.153450307
0.022	-0.306477886
0.044	-0.459364555
0.074	-0.612110315
0.118	-0.764715166
0.203	-0.917038198
0.410	-1.069079411
0.872	-1.223516083
1.721	-1.376684572
3.595	-1.526189416
4.920	-1.677385173
5.292	-1.829426386
6.174	-1.981185781
9.559	-2.127167891
40.364	-2.253563598
78.636	-2.383763858
93.166	-2.520305041

A-2
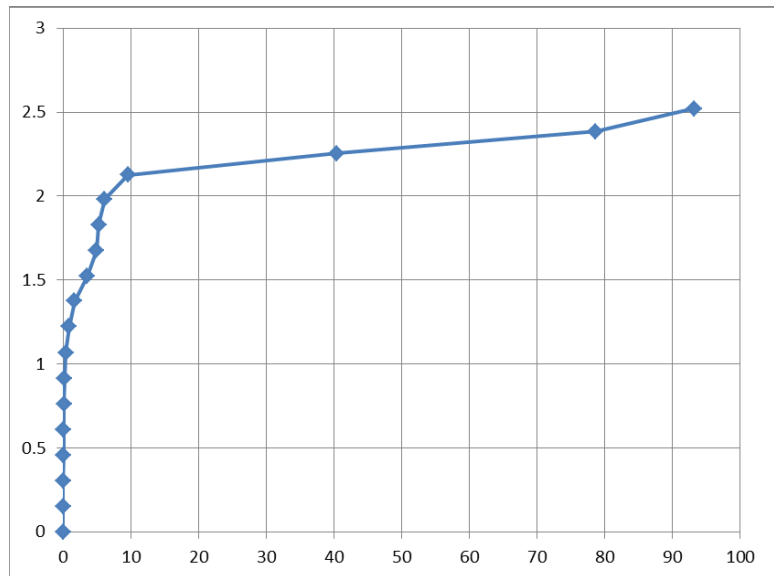
Test02 Data:

Data summary
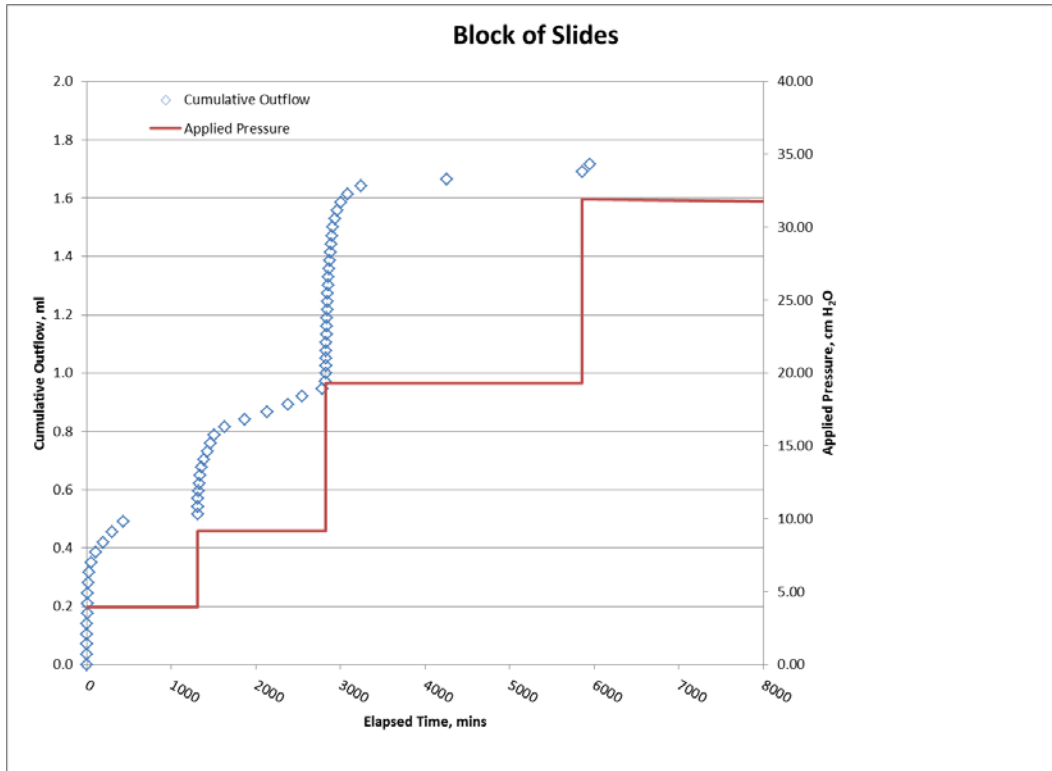
Pressure steps

Elapsed Time (hr)	Pressure (cm H2O)
0	3.977002727
21.82583333	3.977002727
21.82611111	9.1776986
47.06916667	9.1776986
47.06944444	19.27316706
97.57111111	19.27316706
97.57138889	31.91799624
169.8861111	31.61207296

Cumulative flux based on total area

Time (h)	Cumulative flux (cm)
0.000	0.00E+00
0.011	-0.001398118
0.032	-0.002753397
0.054	-0.004108677
0.076	-0.005463956
0.103	-0.00681534
0.136	-0.008170619
0.181	-0.009522004
0.256	-0.0109357
0.404	-0.012290979
0.844	-0.013642364
1.764	-0.014997643
3.284	-0.016352922
5.070	-0.017708201
7.187	-0.019059586
21.855	-0.020076045
21.896	-0.021108082
21.955	-0.022144014
22.034	-0.02318384
22.157	-0.024223667
22.341	-0.025267387
22.639	-0.026326686
23.115	-0.027401562
23.822	-0.028480333
24.462	-0.029566893
25.177	-0.030665137
27.177	-0.031704963
31.218	-0.032721422
35.568	-0.033733987
39.607	-0.034777708
42.472	-0.035790273
46.390	-0.036849571
47.086	-0.037866031
47.10556	-0.038886384
47.12917	-0.039906738
47.15417	-0.040927092
47.18333	-0.041947446
47.21389	-0.0429678
47.25278	-0.044058254
47.29444	-0.045148708
47.33889	-0.046239163
47.3875	-0.047333512
47.44167	-0.048462911
47.50556	-0.049553365
47.58194	-0.05064382
47.66667	-0.051734274
47.76111	-0.052832518
47.87083	-0.053934656
47.99472	-0.055036793
48.14194	-0.05614672
48.32667	-0.057248858
48.55861	-0.058389941
48.87944	-0.059492079
49.33083	-0.060598111
50.06556	-0.061700249
51.435	-0.062810176
54.01417	-0.063920103
70.93556	-0.064780783
97.69222	-0.065766086
99.13	-0.066778651
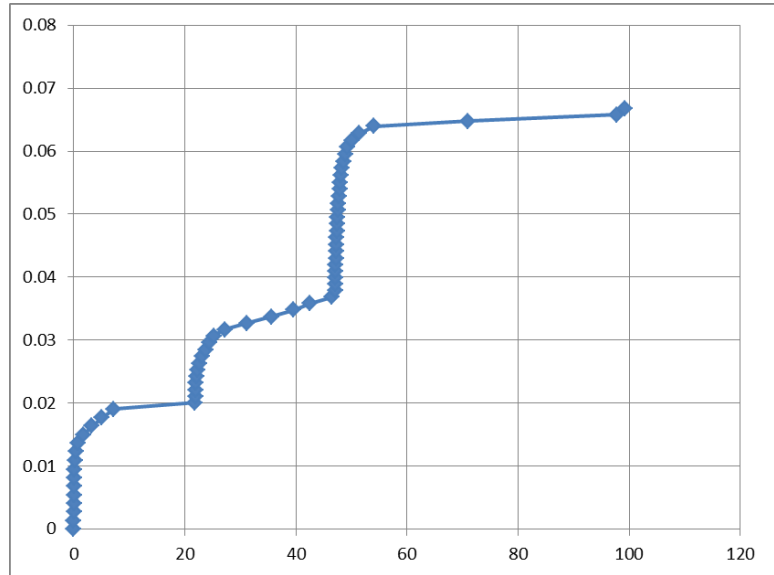
Cumulative flux based on fracture area

Time (h)	Cumulative flux (cm)
0.000	0.00E+00
0.011	-0.050586465
0.032	-0.099622927
0.054	-0.148659388
0.076	-0.19769585
0.103	-0.246591402
0.136	-0.295627864
0.181	-0.344523416
0.256	-0.395673519
0.404	-0.44470998
0.844	-0.493605533
1.764	-0.542641994
3.284	-0.591678456
5.070	-0.640714918
7.187	-0.68961047
21.855	-0.726387816
21.896	-0.7637288
21.955	-0.801210693
22.034	-0.838833496
22.157	-0.876456298
22.341	-0.91422001
22.639	-0.95254736
23.115	-0.991438347
23.822	-1.030470243
24.462	-1.069783958
25.177	-1.109520401
27.177	-1.147143203
31.218	-1.18392055
35.568	-1.220556987
39.607	-1.258320698
42.472	-1.294957135
46.390	-1.333284485
47.086	-1.370061831
47.10556	-1.406980087
47.12917	-1.443898342
47.15417	-1.480816598
47.18333	-1.517734854
47.21389	-1.554653109
47.25278	-1.594107734
47.29444	-1.633562358
47.33889	-1.673016982
47.3875	-1.712612516
47.44167	-1.753476234
47.50556	-1.792930859
47.58194	-1.832385483
47.66667	-1.871840107
47.76111	-1.91157655
47.87083	-1.951453903
47.99472	-1.991331255
48.14194	-2.031490427
48.32667	-2.071367779
48.55861	-2.112654225
48.87944	-2.152531578
49.33083	-2.19254984
50.06556	-2.232427192
51.435	-2.272586363
54.01417	-2.312745535
70.93556	-2.343886506
97.69222	-2.379536577
99.13	-2.416173014
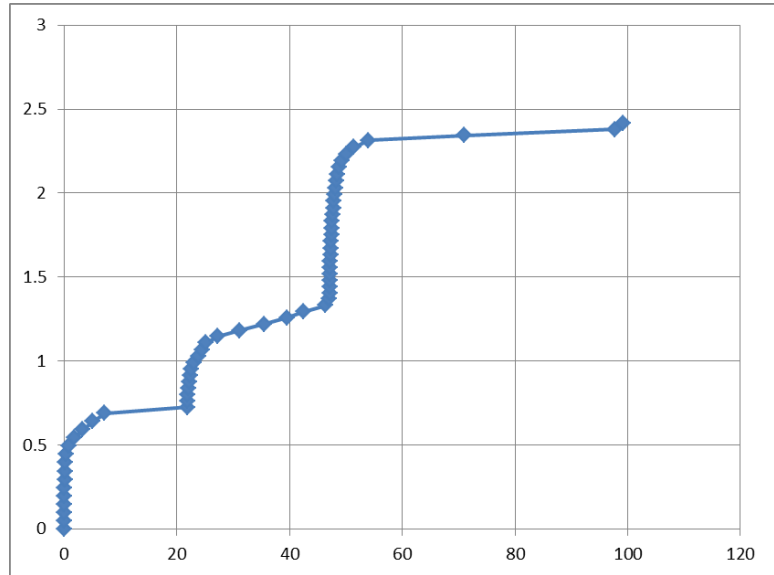
Test04 Data:

Data summary
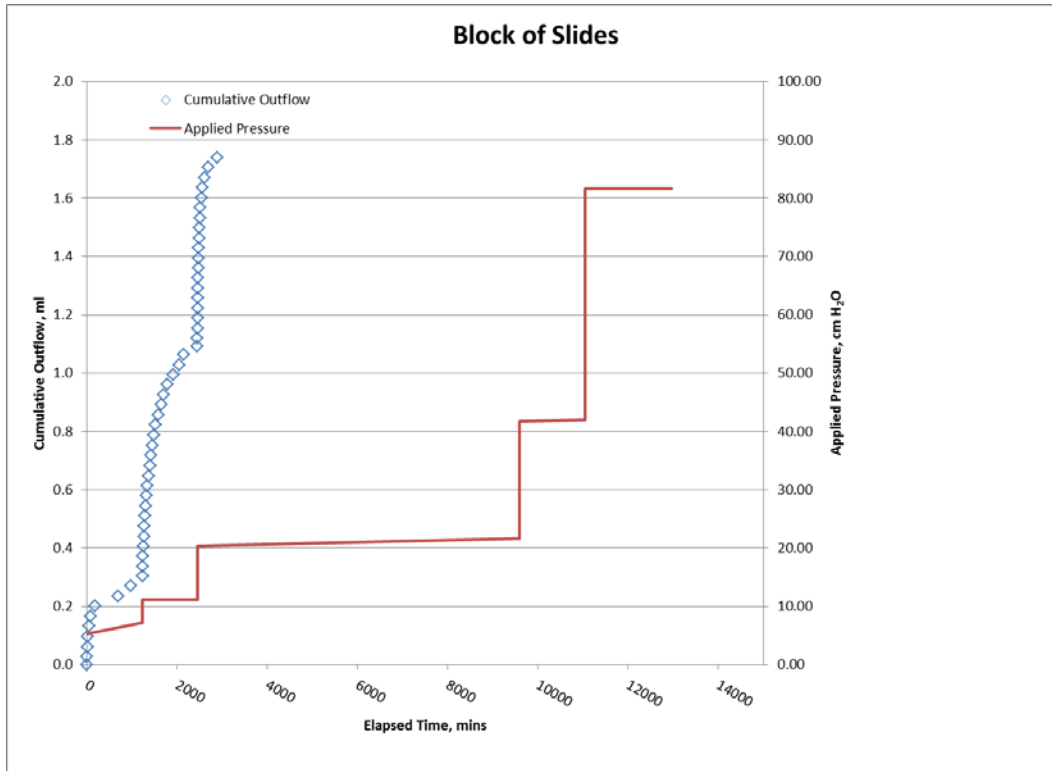
Pressure steps

Elapsed Time (hr)	Pressure (cm H2O)
0	5.302670302
20.57555556	7.138210022
20.57583333	11.11521275
40.94	11.11521275
40.94027778	20.39488578
160.0108333	21.61857893
160.0111111	41.70754142
184.05	41.91149027
184.0502778	81.57954311
215.9744444	81.57954311

Cumulative flux based on total area

Time (h)	Cumulative flux (cm)
0.000	0.00E+00
0.058	-0.001059299
0.179	-0.002418472
0.402	-0.003777646
0.809	-0.005132925
1.458	-0.006492098
2.986	-0.007851272
11.549	-0.00917929
16.245	-0.010511202
20.563	-0.011827536
20.672	-0.013163343
20.801	-0.014491361
20.944	-0.015819378
21.098	-0.017155185
21.276	-0.018487097
21.474	-0.019869638
21.701	-0.021205444
21.965	-0.022537357
22.240	-0.023880952
22.911	-0.025220653
23.299	-0.02655646
23.711	-0.027942895
24.201	-0.029282596
24.739	-0.030622297
25.476	-0.032012627
26.482	-0.033352328
27.562	-0.034692029
28.430	-0.03603173
29.809	-0.037375326
31.929	-0.038703344
34.084	-0.04003915
35.840	-0.041374957
40.894	-0.042492673
40.91944	-0.043587022
40.94861	-0.044926723
40.98194	-0.046266424
41.01944	-0.047598336
41.05972	-0.048938038
41.10694	-0.050277739
41.15833	-0.051613545
41.21944	-0.052953247
41.29028	-0.054300737
41.37639	-0.055640438
41.48194	-0.056976245
41.61528	-0.058331524
41.78611	-0.059671225
42.02222	-0.061007032
42.34583	-0.062346733
42.82917	-0.063686434
43.57361	-0.06503003
44.93333	-0.066373625
48.09	-0.067713326

A-7
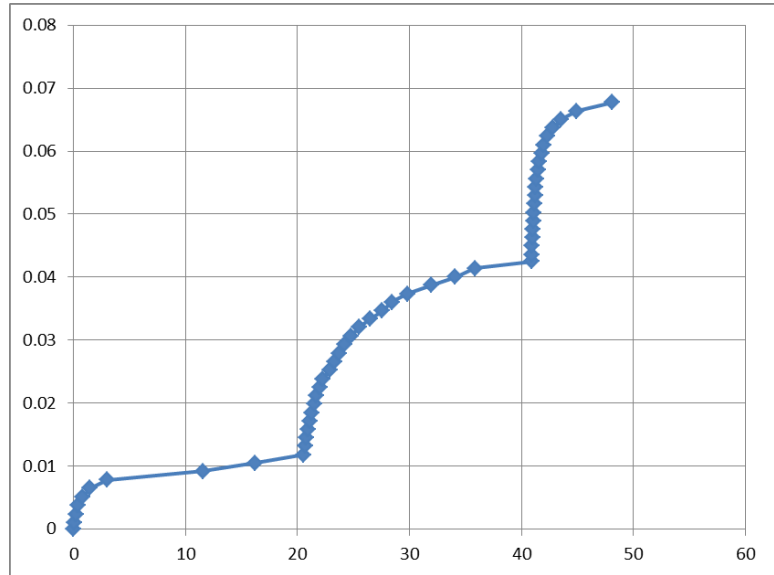
Cumulative flux based on fracture area

Time (h)	Cumulative flux (cm)
0.000	0.00E+00
0.058	-0.038327349
0.179	-0.08750472
0.402	-0.136682092
0.809	-0.185718553
1.458	-0.234895924
2.986	-0.284073295
11.549	-0.332123392
16.245	-0.380314397
20.563	-0.427941765
20.672	-0.47627368
20.801	-0.524323776
20.944	-0.572373872
21.098	-0.620705787
21.276	-0.668896792
21.474	-0.71891962
21.701	-0.767251535
21.965	-0.81544254
22.240	-0.864056274
22.911	-0.912529098
23.299	-0.960861013
23.711	-1.011024749
24.201	-1.059497574
24.739	-1.107970398
25.476	-1.158275044
26.482	-1.206747868
27.562	-1.255220692
28.430	-1.303693516
29.809	-1.35230725
31.929	-1.400357346
34.084	-1.448689261
35.840	-1.497021176
40.894	-1.537462166
40.91944	-1.5770577
40.94861	-1.625530524
40.98194	-1.674003348
41.01944	-1.722194353
41.05972	-1.770667178
41.10694	-1.819140002
41.15833	-1.867471917
41.21944	-1.915944741
41.29028	-1.964699384
41.37639	-2.013172208
41.48194	-2.061504123
41.61528	-2.110540585
41.78611	-2.159013409
42.02222	-2.207345324
42.34583	-2.255818148
42.82917	-2.304290972
43.57361	-2.352904706
44.93333	-2.401518439
48.09	-2.449991264
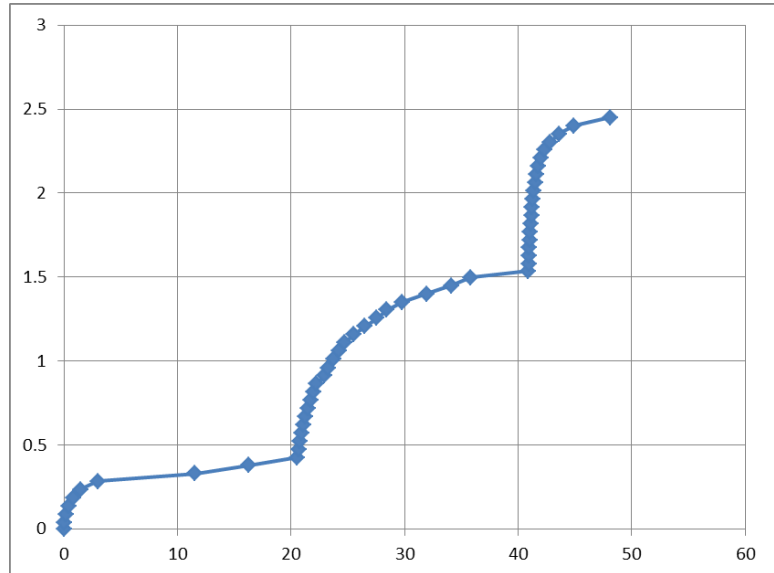
Appendix B. Data from Fractured Grout Experiments

TR436 Data:

Data summary
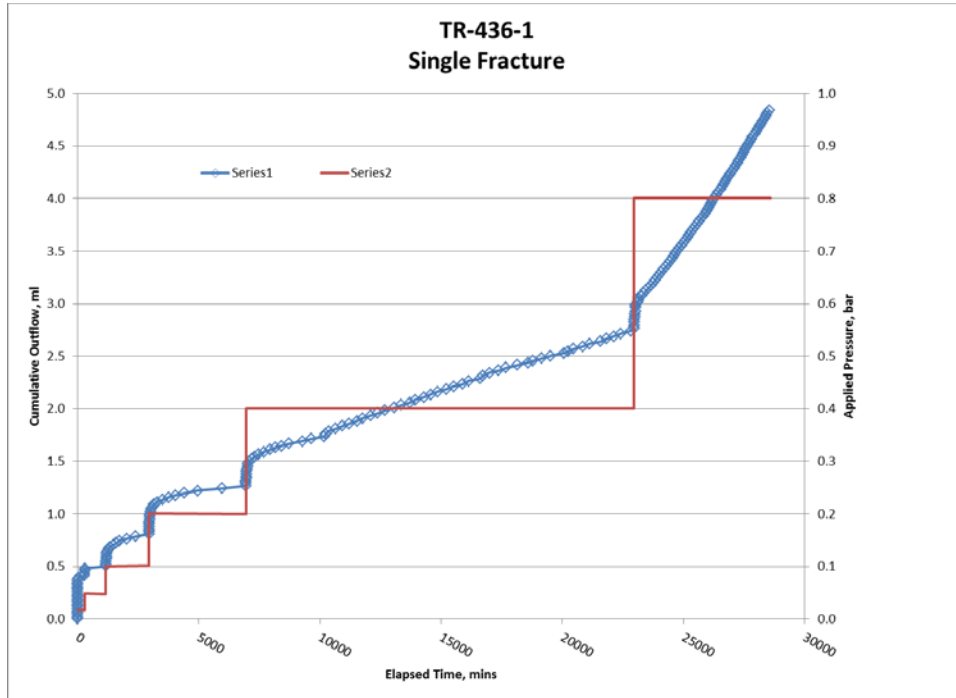
Pressure steps

Elapsed Time (hr)	Pressure (cm H2O)
0.00001	17.23367848
4.716	17.23367848
4.716	49.15167473
19.333	48.94772587
19.333	101.9744289
49.101	103.4020709
49.102	204.8666276
115.835	203.9488578
115.835	408.2036389
382.807	408.2036389

Cumulative flux

Time (h)	Total area flux (cm)	Fracture area flux (cm)
0.0028	-0.00055	-0.03738
0.0042	-0.00109	-0.07492
0.0069	-0.00164	-0.11230
0.0083	-0.00219	-0.14968
0.0111	-0.00273	-0.18706
0.0139	-0.00329	-0.22525
0.0181	-0.00384	-0.26247
0.0236	-0.00438	-0.29969
0.0292	-0.00492	-0.33675
0.0361	-0.00546	-0.37380
0.0444	-0.00601	-0.41102
0.0556	-0.00655	-0.44792
0.0708	-0.00709	-0.48497
0.0931	-0.00763	-0.52235
0.1375	-0.00817	-0.55925
0.2222	-0.00871	-0.59631
0.6014	-0.00926	-0.63385
4.8250	-0.00978	-0.66945
4.9042	-0.01033	-0.70667
5.0347	-0.01086	-0.74324
5.3069	-0.01140	-0.78029
19.4656	-0.01193	-0.81638
19.5489	-0.01246	-0.85263
19.6572	-0.01299	-0.88904
19.7933	-0.01354	-0.92642
19.9683	-0.01407	-0.96299
20.2156	-0.01462	-1.00086
20.6017	-0.01515	-1.03710
21.2683	-0.01568	-1.07303
22.5072	-0.01620	-1.10863
24.6378	-0.01671	-1.14390
26.5892	-0.01706	-1.16785
28.6442	-0.01759	-1.20345
34.1414	-0.01810	-1.23841
40.2136	-0.01862	-1.27449
49.1164	-0.01914	-1.30993
49.1789	-0.01969	-1.34731
49.2469	-0.02023	-1.38469
49.3233	-0.02079	-1.42288
49.4108	-0.02135	-1.46139
49.5150	-0.02190	-1.49861
49.6386	-0.02246	-1.53680
49.7914	-0.02302	-1.57532
49.9844	-0.02358	-1.61367
50.2539	-0.02412	-1.65089
50.6622	-0.02467	-1.68859
51.3886	-0.02521	-1.72532
52.5706	-0.02576	-1.76270
54.8386	-0.02628	-1.79879
58.5011	-0.02680	-1.83423
62.7122	-0.02732	-1.86983
67.2789	-0.02784	-1.90510
73.5608	-0.02837	-1.94168
82.7483	-0.02889	-1.97744
99.2928	-0.02940	-2.01190
115.8417	-0.02991	-2.04670
115.9028	-0.03046	-2.08424
115.9736	-0.03102	-2.12275
116.0583	-0.03156	-2.16013
116.1583	-0.03211	-2.19735
116.2792	-0.03267	-2.23554
116.4306	-0.03321	-2.27276
116.6264	-0.03375	-2.30998
116.9056	-0.03431	-2.34784
117.3569	-0.03487	-2.38603
118.1347	-0.03542	-2.42406
119.7639	-0.03595	-2.46015
121.9653	-0.03649	-2.49720
124.6000	-0.03701	-2.53313
128.1667	-0.03753	-2.56856
132.4403	-0.03805	-2.60417
136.0306	-0.03857	-2.63977
140.3583	-0.03893	-2.66404
145.7014	-0.03947	-2.70093
154.6617	-0.03999	-2.73670
160.7047	-0.04052	-2.77311
169.8700	-0.04109	-2.81178
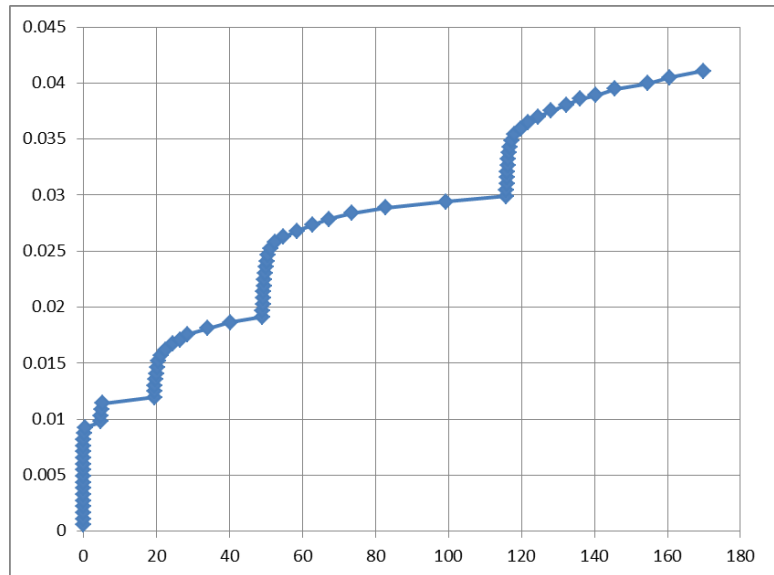
TR437 Data:

Data summary
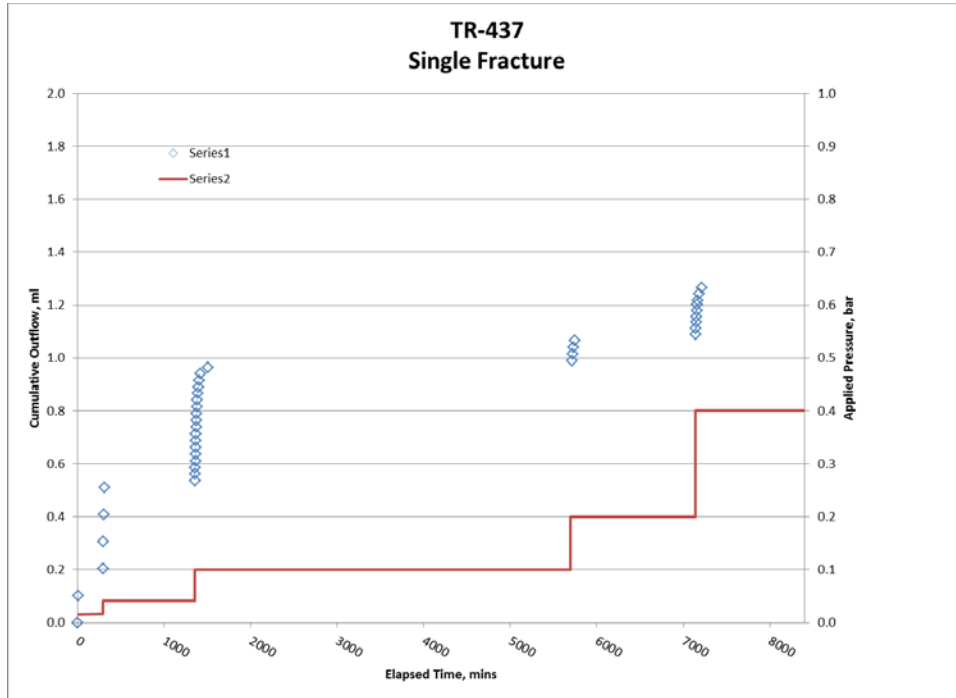
Pressure steps

Elapsed Time (hr)	Pressure (cm H2O)
0.00001	15.90801091
4.854	17.23367848
4.854	41.70754142
22.631	41.70754142
22.635	102.484301
94.883	102.484301
94.883	204.2547811
118.993	204.2547811
118.994	408.1016644
144.094	408.1016644

Cumulative flux

Time (h)	Total area flux (cm)	Fracture area flux (cm)
0.001	-1.00E-05	-5.89E-04
0.154	-0.0024	-0.14147
4.932	-0.0049	-0.28884
4.973	-0.0073	-0.43032
5.056	-0.0098	-0.57768
5.272	-0.0122	-0.71916
22.651	-0.0128	-0.75453
22.67	-0.0134	-0.78989
22.691	-0.014	-0.82526
22.714	-0.0146	-0.86063
22.739	-0.0152	-0.896
22.767	-0.0158	-0.93137
22.798	-0.0164	-0.96674
22.831	-0.017	-1.00211
22.869	-0.0176	-1.03747
22.912	-0.0182	-1.07284
22.959	-0.0189	-1.11411
23.016	-0.0195	-1.14947
23.084	-0.0201	-1.18484
23.17	-0.0207	-1.22021
23.281	-0.0213	-1.25558
23.447	-0.0219	-1.29095
23.745	-0.0225	-1.32632
25.056	-0.023	-1.35579
95.267	-0.0236	-1.39116
95.37	-0.0242	-1.42653
95.513	-0.0248	-1.4619
95.756	-0.0255	-1.50316
119.051	-0.026	-1.53263
119.094	-0.0266	-1.568
119.144	-0.0271	-1.59747
119.205	-0.0276	-1.62695
119.278	-0.0282	-1.66232
119.374	-0.0287	-1.69179
119.459	-0.0291	-1.71537
119.656	-0.0297	-1.75074
120.214	-0.0303	-1.78611
140	-0.0303	-1.78611

B-4
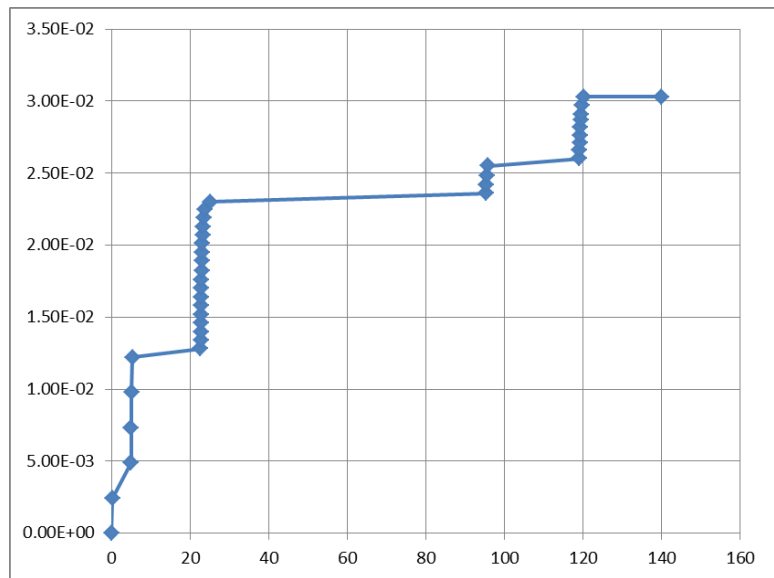
TR430.1 Data:

Data summary
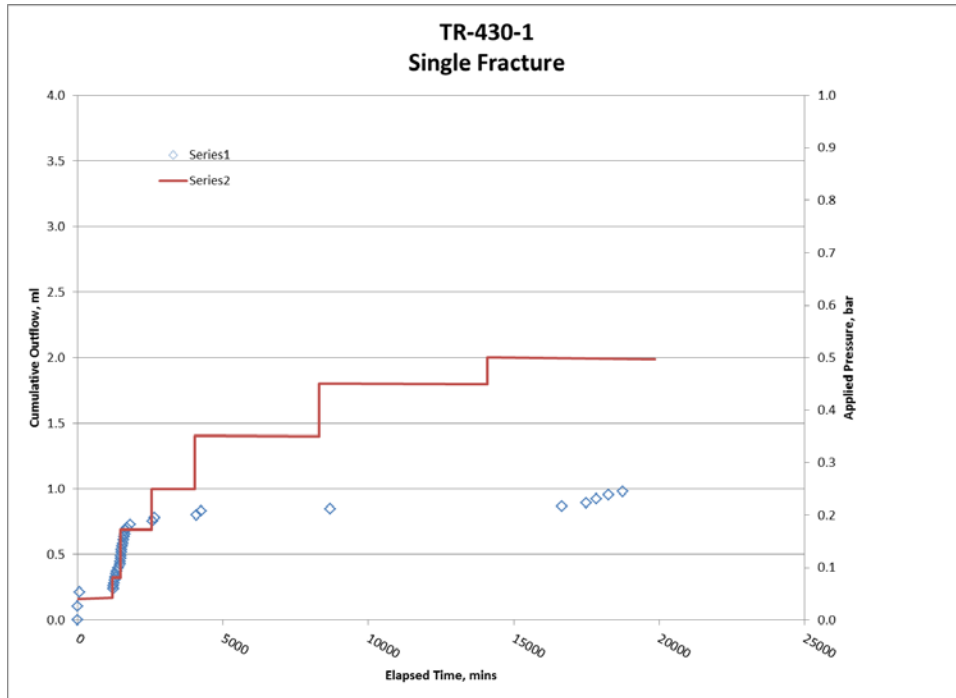
Pressure steps

Elapsed Time (hr)	Pressure (cm H2O)
0.000001	41.09569484
19.78111111	42.82926013
19.78138889	82.08941526
24.43333333	82.08941526
24.43361111	176.1098387
42.325	176.1098387
42.32527778	254.9360722
67.07861111	254.9360722
67.07888889	358.7460408
138.6544444	357.0124756
138.6547222	459.3948022
234.76	457.9671602
234.7602778	510.3820166
330.76	507.1188349

Cumulative flux

Time (h)	Total area flux (cm)	Fracture area flux (cm)
0.043	-2.62E-03	-2.40E-01
1.101	-0.00522	-4.80E-01
20.430	-0.00578	-5.30E-01
20.666	-0.00634	-5.82E-01
20.938	-0.00689	-6.33E-01
21.237	-0.00745	-6.84E-01
21.592	-0.00802	-7.37E-01
22.020	-0.00858	-7.88E-01
22.559	-0.00914	-8.40E-01
23.297	-0.00971	-8.91E-01
24.435	-0.0103	-9.45E-01
24.578	-0.01087	-9.98E-01
24.745	-0.01146	-1.05E+00
24.931	-0.01203	-1.10E+00
25.134	-0.0126	-1.16E+00
25.357	-0.01317	-1.21E+00
25.606	-0.01373	-1.26E+00
25.884	-0.0143	-1.31E+00
26.200	-0.01488	-1.37E+00
26.568	-0.01545	-1.42E+00
27.027	-0.01602	-1.47E+00
27.616	-0.01662	-1.53E+00
28.481	-0.0172	-1.58E+00
30.102	-0.01778	-1.63E+00
43.043	-0.01838	-1.69E+00
44.175	-0.01898	-1.74E+00
68.069	-0.01957	-1.80E+00
70.734	-0.02022	-1.86E+00
144.872	-0.02072	-1.90E+00
277.651	-0.02121	-1.95E+00
291.456	-0.02185	-2.01E+00
297.506	-0.02255	-2.07E+00
304.449	-0.02325	-2.13E+00
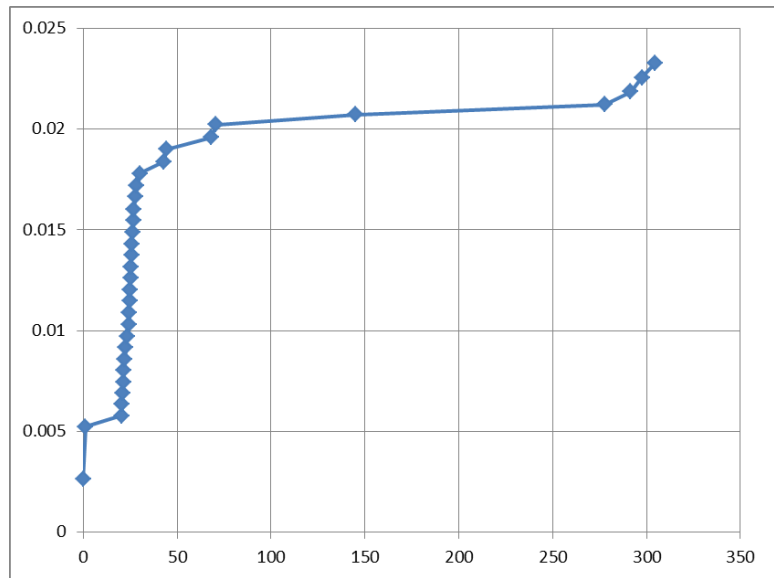
TR430.2 Data:

Data summary
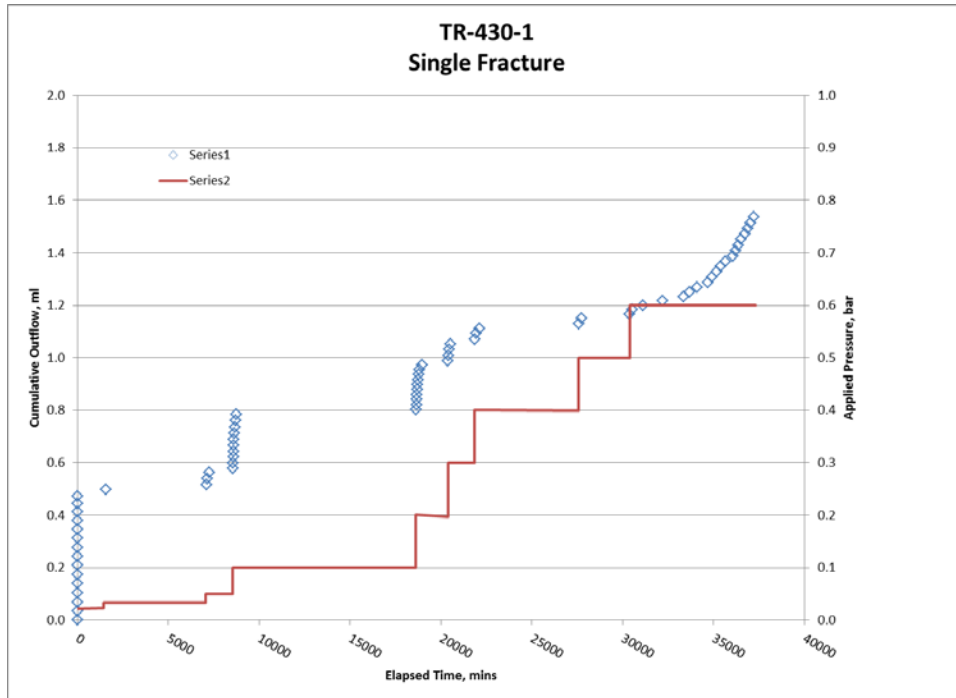
Pressure steps

Elapsed Time (hr)	Pressure (cm H2O)
0	22.33239993
24.11638889	24.06596522
24.11666667	34.16143368
117.4677778	34.16143368
117.4680556	51.29313773
142.4891667	51.29313773
142.4894444	102.0764033
310.4580556	102.0764033
310.4583333	204.3567555
339.685	201.2975226
339.6852778	306.22921
363.9508333	306.22921
363.9511111	408.6115366
459.7302778	407.1838946
459.7305556	510.0760933
506.7602778	509.6681956
506.7605556	612.0505222
621.9802778	611.7445989

Cumulative flux

Time (h)	Total area flux (cm)	Fracture area flux (cm)
0.004	-8.34E-04	-6.18E-02
0.006	-0.00169	-1.25E-01
0.007	-0.00254	-1.88E-01
0.008	-0.00339	-2.51E-01
0.010	-0.00424	-3.14E-01
0.012	-0.00508	-3.77E-01
0.015	-0.00592	-4.38E-01
0.017	-0.00676	-5.01E-01
0.021	-0.0076	-5.63E-01
0.025	-0.00843	-6.24E-01
0.031	-0.00924	-6.85E-01
0.042	-0.01005	-7.45E-01
0.065	-0.01083	-8.02E-01
0.206	-0.01154	-8.54E-01
26.246	-0.01213	-8.98E-01
118.379	-0.01261	-9.34E-01
119.089	-0.01318	-9.76E-01
120.581	-0.01371	-1.02E+00
142.612	-0.01413	-1.05E+00
142.730	-0.01463	-1.08E+00
142.867	-0.01515	-1.12E+00
143.026	-0.01569	-1.16E+00
143.212	-0.01623	-1.20E+00
143.445	-0.0168	-1.24E+00
143.749	-0.01738	-1.29E+00
144.139	-0.01796	-1.33E+00
144.723	-0.01854	-1.37E+00
145.767	-0.0191	-1.42E+00
310.603	-0.01955	-1.45E+00
310.774	-0.02002	-1.48E+00
310.971	-0.0205	-1.52E+00
311.194	-0.02097	-1.55E+00
311.467	-0.02143	-1.59E+00
311.7917	-0.02189	-1.62E+00
312.2181	-0.02236	-1.66E+00
312.8167	-0.02282	-1.69E+00
313.7292	-0.02326	-1.72E+00
315.7653	-0.02369	-1.75E+00
339.8353	-0.02408	-1.78E+00
340.2397	-0.02461	-1.82E+00
340.8522	-0.02516	-1.86E+00
341.9897	-0.02568	-1.90E+00
364.3442	-0.02613	-1.94E+00
365.4469	-0.02664	-1.97E+00
368.8706	-0.02711	-2.01E+00
459.9528	-0.02756	-2.04E+00
462.3875	-0.02804	-2.08E+00
506.1272	-0.02841	-2.10E+00
509.0314	-0.02887	-2.14E+00
518.8619	-0.02928	-2.17E+00
536.425	-0.02967	-2.20E+00
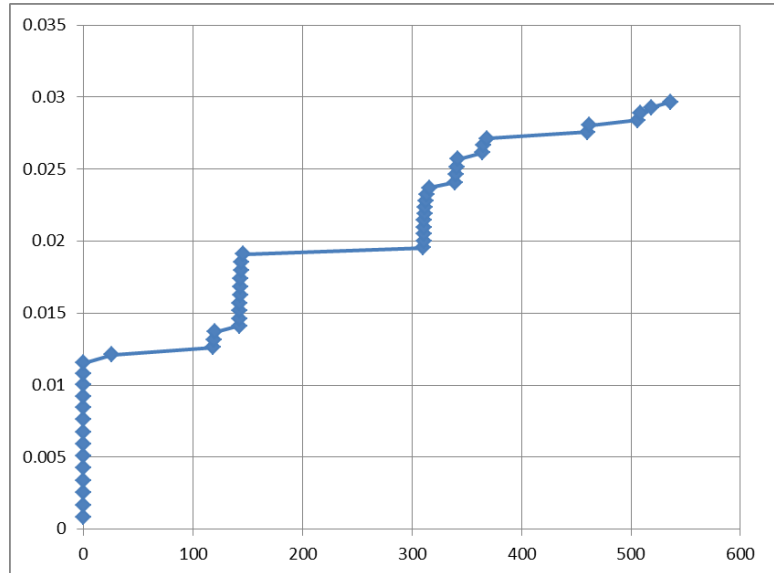
TR430.3 Data:

Data summary
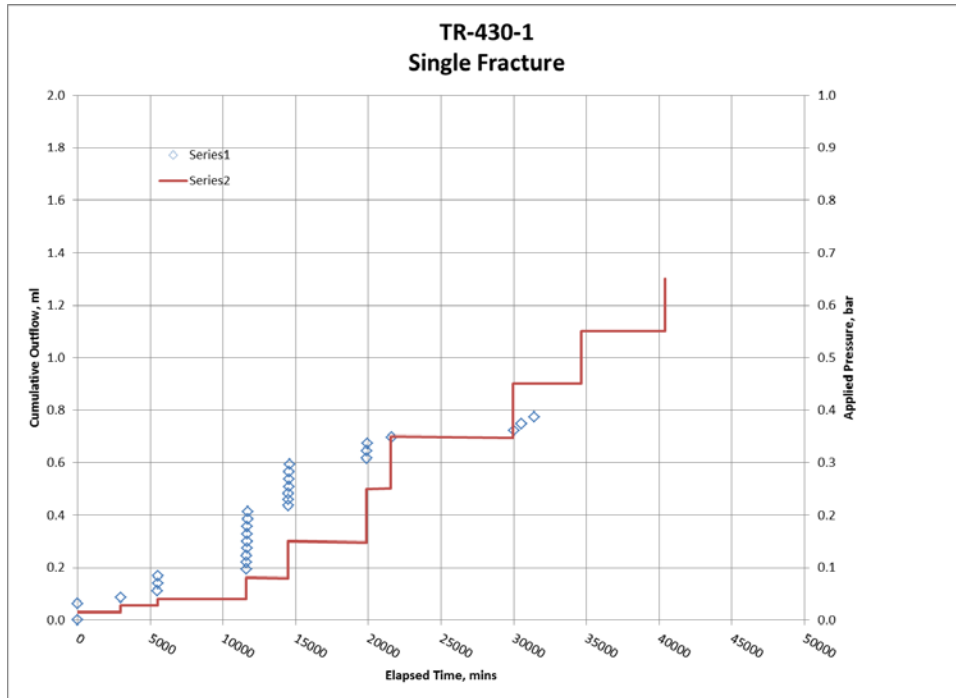
Pressure steps

Elapsed Time (hr)	Pressure (cm H2O)
0.000001	15.70406205
49.08166667	15.70406205
49.08194444	29.16468666
91.54583333	29.16468666
91.54611111	41.09569484
193.5433333	41.09569484
193.5436111	82.08941526
241.6241667	81.78349197
241.6244444	153.4715155
331.0272222	151.228078
331.0275	255.1400211
359.3352778	256.0577909
359.3355556	357.0124756
499.3180556	354.972987
499.3183333	459.7007254
577.085	459.598751

Cumulative flux

Time (h)	Total area flux (cm)	Fracture area flux (cm)
0.179	-1.52E-03	-1.76E-01
49.240	-0.00212	-2.47E-01
91.729	-0.00274	-3.19E-01
91.929	-0.00341	-3.97E-01
92.499	-0.00408	-4.75E-01
193.809	-0.00473	-5.50E-01
193.895	-0.00536	-6.24E-01
193.994	-0.00601	-6.99E-01
194.107	-0.00666	-7.75E-01
194.238	-0.00733	-8.53E-01
194.394	-0.008	-9.31E-01
194.594	-0.00868	-1.01E+00
194.877	-0.00936	-1.09E+00
195.387	-0.01008	-1.17E+00
241.756	-0.01064	-1.24E+00
241.865	-0.0112	-1.30E+00
241.999	-0.0118	-1.37E+00
242.165	-0.01243	-1.45E+00
242.383	-0.01307	-1.52E+00
242.705	-0.01376	-1.60E+00
243.255	-0.01446	-1.68E+00
331.334	-0.01505	-1.75E+00
331.683	-0.01574	-1.83E+00
332.240	-0.01643	-1.91E+00
360.056	-0.017	-1.98E+00
500.567	-0.01759	-2.05E+00
509.149	-0.01827	-2.13E+00
523.320	-0.01889	-2.20E+00
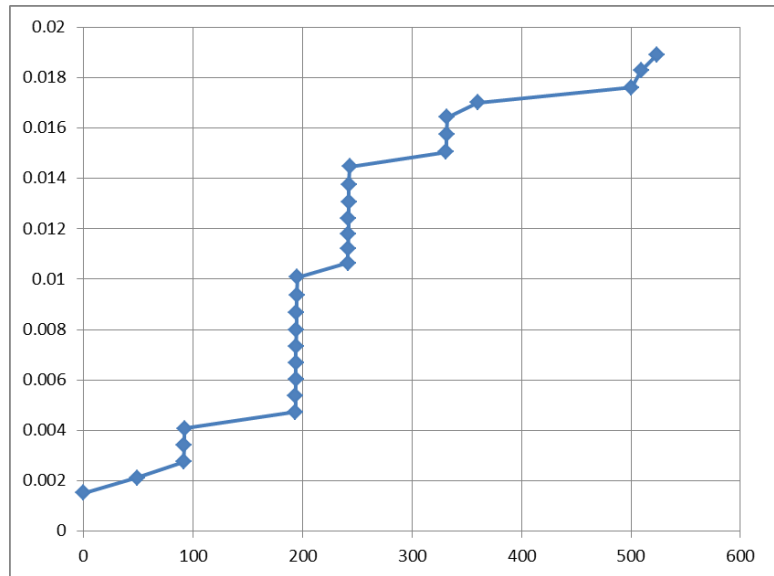
This page intentionally left blank

Distribution:

B. T. Butcher, 773-43A
G. P. Flach, 773-42A
R. A. Hiergesell, 773-43A
M. A. Phifer, 773-42A
R. R. Seitz, 773-43A
F. G. Smith, III 703-41A
G. A. Taylor, 773-43A
T. Whiteside, 773-42A
L. L. Hamm, 735-A
H. H. Burns, 773-41A
E.N. Hoffman, 999-W
D. A. Crowley, 773-43A
T. O. Oliver, 773-42A
J. J. Mayer, 773-42A
K. M. Kostelnik, 773-42A
J. C. Griffin, 773-A
S. L. Marra, 773-A
K. H. Rosenberger, 705-1C
J. E. Mangold, 705-1C
Records Administration (EDWS)